©Copyright by Seyed Mohammad Sajadi 2016
All rights Reserved

Micro-Nano Structures for Tuned Heat Transfer

A Thesis

Presented to

The Faculty of the Department of Mechanical Engineering

University of Houston

In Partial Fulfillment

Of the Requirement for the Degree

Master of Science

In Mechanical Engineering

By

Seyed Mohammad Sajadi

December 2016

Micro-Nano Structures for Tuned Heat Transfer

Seyed Mohammad Sajadi

Approved:

Chair of the Committee
Hadi Ghasemi, Bill D. Cook Assistant Professor,
Mechanical Engineering

Committee Members:

Haleh Ardebili, Bill D. Cook Associate Professor
Mechanical Engineering

Daniel Araya, Assistant Professor
Mechanical Engineering

Suresh K. Khator, Associate Dean,
Cullen College of Engineering

Pradeep Sharma, Professor and Chair,
Mechanical Engineering

Acknowledgment

Firstly, I would like to express my sincere gratitude to my advisor, Dr. Hadi Ghasemi for the continuous support of my Masters study, for his patience, motivation, and immense knowledge. His guidance helped me in all the time of research and writing of this thesis. He taught me the value of hardwork and an education. Without him, I may never have gotten to where I am today.

Next, I need to thank all the people who create such a good atmosphere in the lab, Nazanin Farokhnia, Peyman Irajizad, and Munib Hasnain and other members of NanoTherm lab, have been always there to listen and give advice. I am deeply grateful to them for the discussions that helped me sort out the technical details of my work.

Above all I would like to acknowledge the tremendous sacrifices that my parents made to ensure that I had an excellent education. For this and much more, I am forever in their debt. It is to them that I dedicate this dissertation. To my family, I thank my parents, brother, and sister for supporting me emotionally and mentally when I got stuck or needed reclusion.

Micro-Nano Structures for Tuned Heat Transfer

An Abstract

of a

A thesis

Presented to

The Faculty of the Department of Mechanical Engineering

University of Houston

In Partial Fulfillment

Of the Requirements for the Degree

Master of Science

In Mechanical Engineering

By

Seyed Mohammad Sajadi

December 2016

Abstract

In this thesis, two different projects are reported in two chapters. The first chapter describes solar steam generation by heat localization method. Herein, we worked towards the generation of high pressure steam using heat localization which can be used in small scale power generation units. The development of the corresponding material structure used in the generation of steam has also been reported in this chapter. The second chapter illustrates the thermal management of high temperature system with suppression of Leidenfrost phenomena. Here, we report a material paradigm which increases the Leidenfrost point (LFP) substantially compared to other state of the art approaches and we also substantiate the corresponding theoretical results with simulations and experimental results.

Table of Contents

List of Figures

List of Tables

Nomenclature

Term	Definition
PDMS	Polydimethylsiloxane
DLS	Double-layer Structure
HCL	Hydrochloric Acid
LFP	Leidenfrost Point
AAO	Anodic Aluminum Oxide

Chapter 1

Flexible Artificially Networked Structure for

Ambient/High Pressure Solar Steam Generation

Abstract

Heat localization approach has promised a new route of solar steam generation with higher efficiency than the current bulk heating approaches. In this approach, the material structure localizes the absorbed solar energy, forms a hot spot, and wicks the fluid to the hot spot for steam generation. Non-equilibrium nature of this approach minimizes energy losses leading to its superior performance to the equilibrium approaches. However, so far, the generated steam is only in the ambient pressure, not suitable for high-pressure applications. Here, we report development of a flexible artificially networked material structure highly efficient for ambient and high pressure steam generation with integrity for large-scale and various geometry implementation. The structure generates steam in the temperature range of 100-156 ^{o}C and pressure of 100-525 kPa under the solar irradiation. This material structure promises a robust and highly efficient approach for solar steam generation.

1. Introduction

Among renewable energy resources, solar irradiation is the most abundant resource and can in principle supply multiple of the global energy needs.[1–3] Efficient harvesting of solar energy for steam generation is a key factor in a wide range of applications including solar power generation, absorption chillers, and desalination system to compact applications such as water purification, sterilization, and hygiene systems and even food processing.[4–7] The solar steam generation has a critical footprint on the economical development and health systems in remote areas where sun is the only abundant source of energy.

Currently, methods of steam generation through solar energy use an intermittent medium such as surface or cavity to absorb radiative energy and transfer this energy to the bulk fluid. Thus, the steam generated is in thermal equilibrium with the bulk fluid. This approach leads to significant losses by the optical systems and the hot bulk liquid. New concepts such as volumetric receivers and nanofluids are studied to provide a uniform temperature in the bulk fluid and consequently minimize the surface losses by the bulk heating methods.[8–13] Localization of heat on the surface of nanoparticles suspended in a cold bulk fluid is shown as a viable non-equilibrium approach for steam generation.[14–22] Neumann et al. and other researchers have succeeded to generate steam through this approach with high intensity electromagnetic illumination in magnitude order of 103 kWm^{-2}.[23–26] Although this non-equilibrium approach leads to low heat losses to the cold bulk fluid, the high concentration of electromagnetic irradiation limits the efficient implementation of this approach and applicability for stand-alone compact systems.

Furthermore, high optical concentration adds complexity and cost to the solar thermal conversion systems.

Recently, an approach and corresponding material structure was developed that implemented the heat localization concept at the liquid-vapor interface rather than internal of bulk cold liquid. The developed structure called, double-layer structure (DLS), leads to steam generation at higher efficiency (~%85) and at much lower concentration intensities ($10\ kWm^{-2}$) compared to the other methods.[27] This approach paves the way for efficient implementation of solar steam generation in a wide range of disciplines. Recently, other new materials structures such as plasmonic films, carbon black films, porous Graphene, polypyrrole (PPy) coated stainless steel mesh, and thin-film black gold membrane are also suggested for solar steam generation.[28–34] However, the generated steam by all of these structures is at ambient pressure (1 atm) and cannot be utilized in high-pressure applications such as power generation, absorption chillers, and autoclave sterilization systems. In addition, the rigid nature and cost of these structures adversely affect their large scale and various geometry implementations.

Here, we report development of a flexible artificially networked material structure for solar steam generation in both ambient and high pressures with higher efficiency than other state-of-the-art structures. The developed structure is a porous polymer structure with artificial veins and is fabricated in a two-step process needed to achieve the required thermal and hydrodynamic properties. The fast dynamics of wetting, low thermal conductivity, and high absorption in the solar spectrum lead to superior performance of

this structure for steam generation. The flexibility and integrity of this structure allows for facile large-scale implementation.

2. Material Structure

A robust material structure for heat localization at the liquid-vapor interface needs to possess five characteristics:

- Highly absorbing in the solar spectrum
- Buoyant at the liquid surface
- Low thermal conductivity for heat localization
- Fast dynamics of wetting for continuous fluid transport to the liquid-vapor interface
- Integrated and flexible for large-scale implementation.

High absorption in the solar spectrum, buoyant behavior, and low thermal conductivity allows to localizes the irradiated thermal energy near the liquid-vapor interface and generate a hot spot. The fast dynamics allows to transport the liquid driven by capillary action to this generated hot spot for localized steam generation. To achieve these characteristics, we developed a two-step process for fabrication of this structure. The schematic of the process is shown in Fig. 1. Polydimethylsiloxane (PDMS) was chosen as the skeleton of this material structure to provide the flexibility, buoyant nature of the structure on the fluid surface, and low thermal conductivity. We used high internal phase emulsion approach for development of this porous skeleton (APPENDDIX I).[35,36] This porous skeleton is covered with exfoliated graphite flakes [37,38] to provide high absorptivity in the solar spectrum (i.e. absorptivity of >97%). The porous polymer skeleton leads to low thermal conductivity of the structure for heat localization. To achieve fast dynamic of wetting, the structure needs to have a network of veins for transport of fluid.

We have artificially made these veins for transport of the fluid. Scarifying aluminum foam is utilized to induce these veins. We examined three types of foam to find the best-networked structure for solar steam generation. The detailed procedure of development of this material is provided in the APPENDIX I and APPENDIX II.

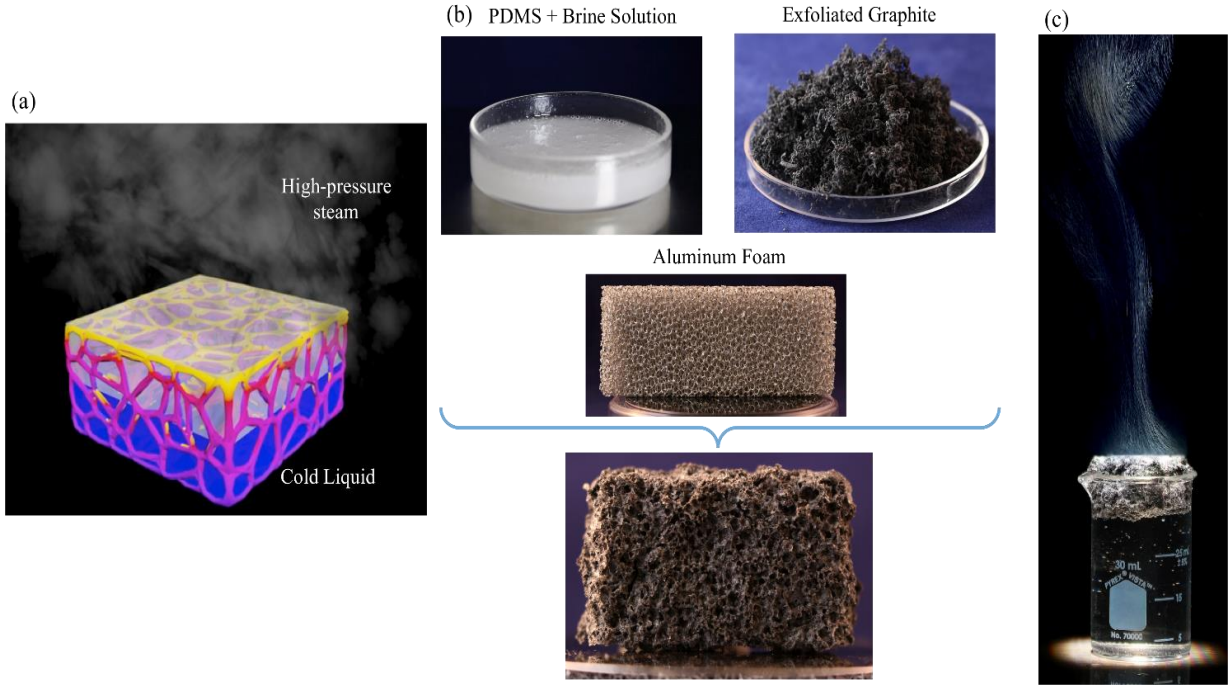

Figure 1. (a) A schematic of the flexible artificially networked structure (b) The components include PDMS+Brine solution, exfoliated graphite, and the scarifying aluminum foam. (c) While the bulk of the fluid is cold, the steam is generated at the surface of this structure at both ambient and high pressures.

2.2. Characterization of the Material

The developed structure should have a range of characteristics for solar steam generation as shown in Fig. 2. The radiative absorption of exfoliated graphite in the solar spectrum (0.25-2.5 μm) is already examined in our previous work [27]. Exfoliated graphite has absorptivity of more than 97% in this wavelength spectrum. We measured porosity of the developed material structure through fluid displacement approach. The porosity of this

structure is to 53 ± 3 %. The detail of the experimental approach is given in (APPENDIX III). The buoyant characteristic of this structure is resulted from low density of porous PDMS skeleton as shown in **Fig. 2a**. The next required characteristic of this structure is fast dynamics of wetting. This dynamics depends on the radius of the artificially developed veins in the structure (R) and the contact angle of the fluid on the walls of these veins (θ). The dynamics of fluid transport in these veins consists of two regions: inertia dominant region and viscous dominant region. As the radius of the veins is in the micron range and the thickness of the structure is in the centimeter range (i.e. length-scale for fluid transport), inertia dominant region (i.e. entry length) is much smaller than the viscous dominant region. Thus, we have assumed the fluid transport is viscous dominant flow derived by the capillary force. To determine the dynamics of the fluid transport in the structure, we placed a water droplet on the surface and examined its dynamics as it impregnates the structure as shown in **Fig. 2b**. Through the analysis given in the APPENDIX IV, the calculated radius of the artificially developed veins is 30 ± 10 μm and the velocity of the fluid at the surface of this structure is ~ 10 cm/s. If we consider an extreme case in which all the irradiated solar energy is consumed in the phase-change process, given the velocity of the fluid transport to top of the structure, the developed material structure sustains the continuous fluid transport even up to 10^5 kWm^{-2} electromagnetic illuminations without drying. This is an important characteristic of the structures for solar steam generation utilized at high solar concentrations.

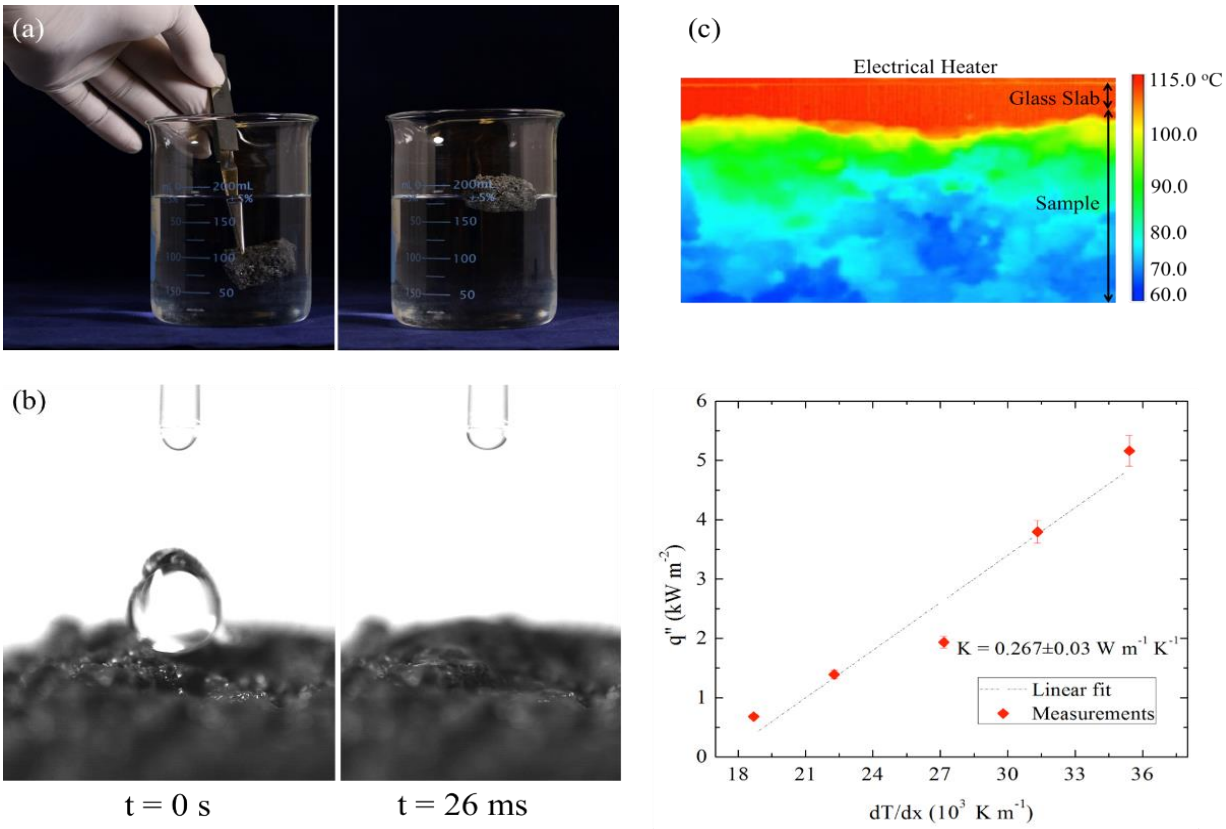

Figure 2. (a) The structure is buoyant on the water surface. (b) The dynamics of wetting of the structure is shown. Once fluid touches the surface of the structure, it is driven to the structures through capillary interaction. (c) The thermal conductivity of the structure is examined with IR method.

The thermal conductivity of this structure is measured with an IR method. The detail of this method is given in the (APPENDIX V). The measured thermal conductivity of the structure is 0.267 ± 0.03 $Wm^{-1}K^{-1}$ as shown in **Fig. 2c**. As the developed structure is one integrated structure with a porous polymer skeleton, it is flexible and can be implemented in different geometries. Furthermore, we examined mechanical, thermal and chemical stability of the developed structure. For the mechanical and thermal stability, we conducted long-time high-pressure tests reported below. These tests were conducted for more than 24 hrs. No change in the structural integrity and performance of the structure

was detected. For chemical stability, the material structure was soaked in a range of solutions with PH range of 1-11 for more than 18 hrs (APPENDIX VI). No change in structural integrity was detected.

3 Performance of the Structures

Once we characterized the properties of this structure, we used the developed experimental setup discussed in the (APPENDIX VII) to assess performance of this structure for solar steam generation. We conducted two sets of experiments: ambient pressure experiments and high-pressure experiments. For both of these experiments, we used the same experimental setup. As diameter of the solar spot is only 25.4 mm, the 2D side losses are significant (38-44%, APPENDIX VIII, **Fig. 9**.). Thus, we conducted ambient pressure experiment with the developed samples herein, pure graphite, and previously reported DLS and determined the relative efficiencies. The relative efficiency ($\Delta\eta$) is defined as

$$\Delta\eta = \eta - \eta_{DLS}, \quad (1)$$

where η_{DLS} denotes the efficiency of double-layer structure, the state-of-the-art structure for localized solar steam generation.

3.1 Ambient Pressure Experiment

The results of the ambient pressure experiments are shown in **Fig. 3**. First, we examined the performance of these structures in the solar concentration of 24 kWm^{-2}. The relative efficiency is shown in **Fig. 3a**. As shown, the sample S1 and S2 have efficiency in the same range as other previously reported values. However, sample S3 outperforms all other structures. In sample S3, the introduced scarifying aluminum foam was 20 PPI with density of 7-9%. That is larger pore size compared to S1, and the lower density of channels compared to S2 leads to this high superior performance. We tried aluminum foams with

larger pore size (e.g. 10 PPI), but the low density of the developed network adversely affected the performance of the structure. Once the optimal networked veins was found, we conducted the ambient pressure experiments at a range of solar concentrations and compared the performance of S3 networked structure with the exfoliated graphite and DLS. As shown, the S3 structure outperforms the other structures, especially at high solar concentrations. The energy conservation at the surface of the structure requires that the irradiated solar power converts to the three forms of energy: (i) enthalpy of phase-change, (ii) energy dissipated through surface convection, radiation, and heat losses to the experimental setup, (iii) energy conducted to the underlying liquid. The energy consumed in category (i) and (ii) are only a function of temperature of the structure (i.e., close to temperature of the generated steam). As temperature of the generated steam in all the samples at ambient pressure is ~100 ^{o}C (APPENDIX VIII, **Fig. 8**.), the only difference in the efficiency should be related to the heat loss to the underlying liquid. We have measured the temperature rise of the underlying liquid as a function of time and plotted for different structures at a range of solar concentrations. The results are shown in **Fig. 3c**. and indicate that the structure S3 is the most efficient structure for limiting the energy loss to the underlying liquid. In other words, the structure S3 outperforms the other structures in heat localization and consequently higher efficiency for solar steam generation. These heat localization characteristics are also determined through temperature measurement at both sides of the S3 structure, one in the steam generated and the other one in the underlying liquid of the structure. These measurements for a long period of time are shown in **Fig 3d**.

As shown, upon the solar irradiation, the structure localizes the energy at top and generates steam while the liquid underlying the structure is at cold temperature.

This non-equilibrium steam generation is achieved by the discussed characteristics of the material structure.

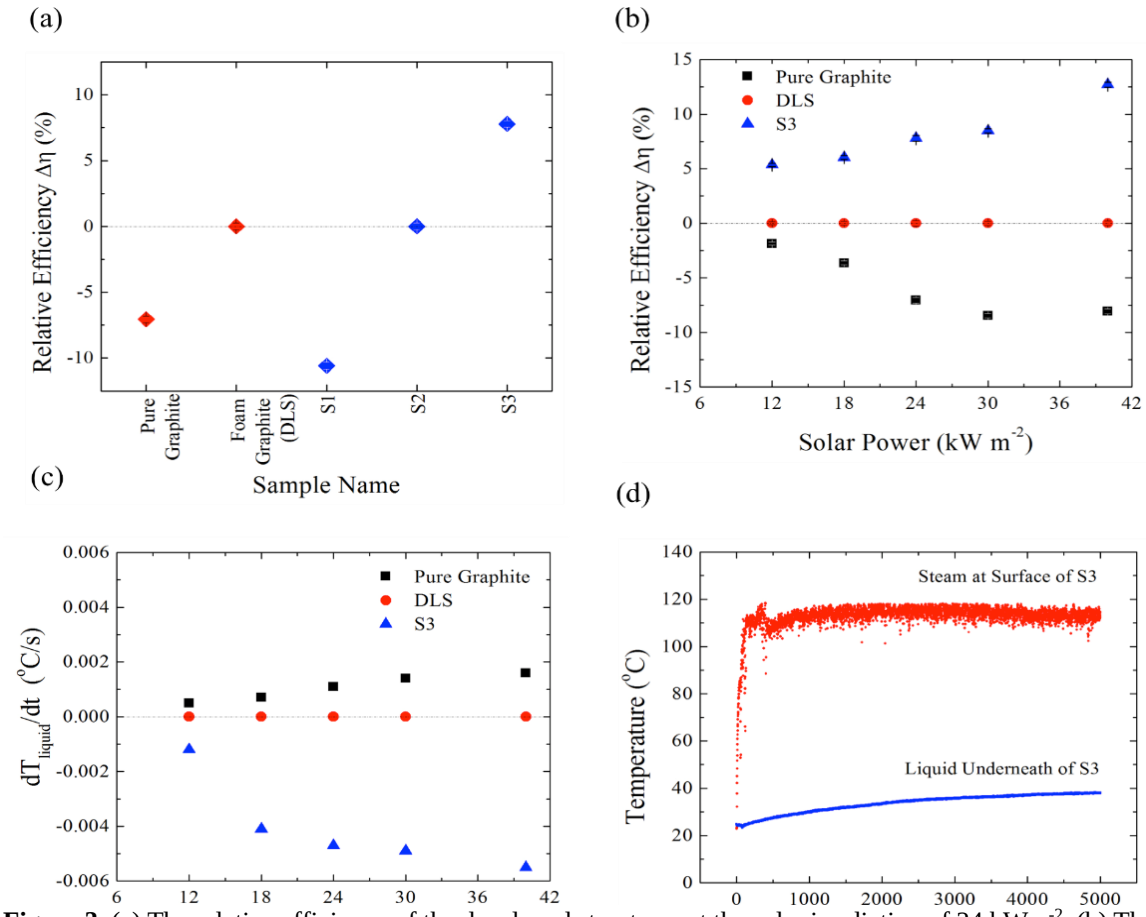

Figure 3. (a) The relative efficiency of the developed structures at the solar irradiation of 24 kWm^{-2}. (b) The performance of the flexible networked structure at a range of solar irradiation. (c) The rate of temperature rise of the underlying liquid for different structures at a range of solar irradiations (d) The non-equilibrium of solar steam ,while steam is generated at the surface, the bulk liquid is cold.

3.2 High Pressure Experiment

The next objective of this study is to generate high-pressure steam required in a wide range of applications including power generation, hygiene systems, and solar cooling technologies. The developed experimental setup is specially designed to address this type of experiments. The experimental setup can withstand up to 1.04 MPa. The detail of these experiments is provided in the (APPENDIX VII). The results of these experiments are shown in **Fig. 4**. We measured pressure of the generated steam at a range of solar concentration shown in **Fig. 4a**. At high solar concentration (50 kWm^{-2}), we continued the experiments for more than 24 hrs to examine the long-term performance of the structure. As shown, no change in the performance of the structure is detected. Also, the material structure remains intact after the experiments indicating its mechanical and thermal stability. At high pressure, the buoyant structure at the liquid-vapor interface experiences a compression force by the liquid and the steam. This compression may affect configuration of the networked structure and consequently liquid transport to the liquid-vapor interface. However, continuous pressure rise indicates constant capillary driven force for transport of liquid to the liquid-vapor interface. Note that the capillary pressure is only a function of dimension of the veins in the structure and is independent of the fluid pressure. To assure heat localization by the structure even at the high pressure, we measured temperature of the liquid underneath of the structure after 24 hrs under the solar concentration of 50 kWm^{-2}, which was 55 ^{o}C. That is, heat localization at the liquid-vapor interface is achieved even at high pressures. Considering saturation condition at the surface of the structure (156 ^{o}C), the conduction heat loss through the structure to the underlying

liquid is only 3.6%. Note that thickness of the structure is 15 mm. The convection and radiation losses from the surface of the structure at 156 ^{o}C are approximately 5.2%. That is, 91.2% of the irradiated energy is consumed for the solar steam generation. While the high-pressure steam is generated, we video recorded the surface of the structure. Boiling occurs at the surface of the structure indicating the saturation state of the generated steam. This boiling is shown in inset of **Fig. 4b**. Through the measured pressure of the steam, we have plotted the corresponding temperature of steam at the given range of solar concentration in **Fig. 4b**. The results suggest that the structure can generate high pressure and temperature steam in the range of 100-156 ^{o}C and 100-525 kPa. To the extent of our knowledge, this is the first reported high-pressure steam generation through heat localization approach.

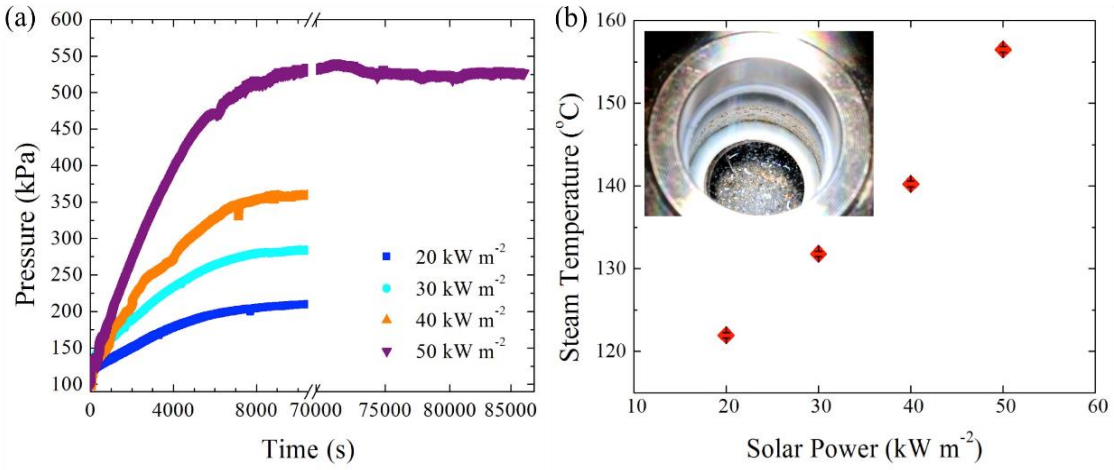

Figure 4. (a) The steam pressure as a function of solar concentration is shown. (b) The corresponding steam temperature as a function of solar concentration is shown. The inset photo shows the fluid at surface of the structure is at the boiling state.

4. Conclusions

We have developed a new flexible artificially networked material structure for solar steam generation at both ambient and high pressures through heat localization. The porous skeleton of this structure makes the structure buoyant at the liquid-vapor interface and reduces its thermal conductivity for heat localization. The exfoliated graphite flakes on this skeleton absorb the broad-bond solar illumination and localizes the solar energy in a hot spot in this structure. The developed 3D artificial veins efficiently transport the fluid to this hot spot for steam generation. This structure outperforms the other reported structures in heat localization and consequently leads to higher efficiency in solar steam generation. The generated steam with this structure ranges from 100-156 ^{o}C with pressure of 100-525 kPa. This is the first reported solar steam generation at high pressure through heat localization approach. This work opens a new path to implement heat localization approach in high temperature/pressure applications including power generation, cooling systems, and hygiene devices.

APPENDIX

APPENDIX I: Synthesis of the flexible artificially networked structure for steam generation

The Polydimethylsiloxane (PDMS) was obtained from Cone Elastomer (Kit 184SIL). The hardener in the ratio of 1:10 was added to the PDMS and mixed thoroughly. We used the internal phase emulsion approach to develop a highly porous PDMS skeleton. Brine with 1:1 ratio is added to PDMS and thoroughly mixed to make a saturated emulsion. The diameter of the dispersed water droplets in the emulsion varies in a wide range of length-scale. These droplets leave the structure through evaporation in polymerization process leading to a highly porous polymer skeleton (see **Fig. 6**). The acid-washed graphite flakes are obtained from Ashbury Carbons with product number of 3772. These flakes were heated in a microwave for 10-15s to achieve high-surface area fluffy exfoliated graphite. Further treatment with microwave did not affect hydrophilicity of the graphite flakes. The trapped gases between the graphite layers expand in the heating process and detach the flakes from each other. The volumetric exfoliation during this process is approximately 100 times. The fabricated graphite was added to the PDMS solution and mixed in the ratio given in Table 1. To achieve highly-interconnected artificial veins in the structure, we used scarifying aluminum foam. The aluminum foam was purchased form K. R. Reynolds company (Duocel Aluminum Foam). Three types of the foam were examined in this work, 20 PPI and 40 PPI (pore per inch) with different density as shown in Table 1. The foam was impregnated with the developed solution of graphite and PDMS. The foam was placed in the oven for one hour at 110 ^{o}C. After curing of the PDMS skeleton, the aluminum foam

was dissolved by soaking the structure in hydrochloric acid (HCL) 35-38%. The dissolving process takes around 48-72 hrs. The final structure was washed with distilled water.

Table 1 . Specification of the studied flexible artificially networked structures

Sample	PDMS [mL]	Brine [mL]	Graphite [mg]	Aluminum Foam
S1	5.5	5.5	0.2	40 PPI (7-9% Density)
S2	5.5	5.5	0.2	20 PPI (13-15% Density)
S3	5.5	5.5	0.2	20 PPI (7-9% Density)

APPENDIX II: Development of the Porous Polymer Skeleton

The highly porous PDMS skeleton is developed through high internal phase emulsion approach. To show the scale of porosity through this approach, we fabricated the samples of pure porous PDMS as shown in **Fig. 5**. This structure is achieved through mixing of brine and PDMS with ratio of 1:1. The mixed solution is cured in the oven at 110 ^{o}C for one hr.

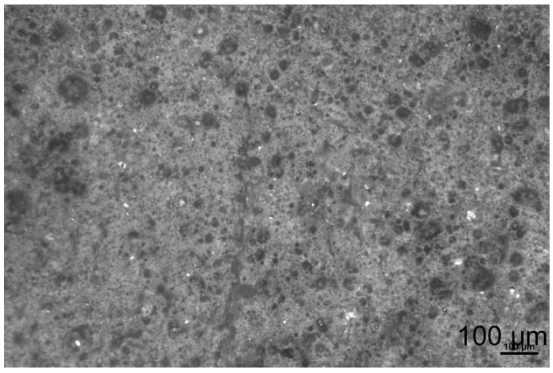

Figure 5. The structure of porous PDMS is shown. The structure includes pore sizes in the range of 2-100 µm. These pores make the structure buoyant and reduce its thermal conductivity.

APPENDIX III: Porosity Measurements

We used fluid saturation approach to measure porosity of the structure. First, the mass of the dry sample was measured (m_1). Next, we filled the structure with isopropyl alcohol and measured the saturated mass of the structure (m_2). Low surface tension of isopropyl alcohol allows for complete wetting of the veins inside the structure. The mass of fluid in the pores is written as ($m_p=m_2-m_1$). Then, volume of the pores is written as $V_p = m_p/\rho_{iso}$, where ρ_{iso} denotes the density of isopropyl alcohol (792 kgm^{-3}). In the third step, we immersed the saturated structure in a bath of isopropyl alcohol and measured the buoyancy force imposed on the structure (W_3). The choice of isopropyl alcohol allows the structure to become completely immersed in the bath to avoid any uncertainty in the buoyancy force measurements. The volume of the structure (V_s) is written as

$$V_s = \frac{W_3/g}{\rho_{iso}}, \tag{A1}$$

thus, the porosity of the structure is written as

$$Porosity = \frac{V_p}{V_s}, \tag{A2}$$

we measured the porosity of S3 structure in five independent measurements. The measured porosity is 53 ± 3 %.

APPENDIX IV: Dynamics of Wetting

The dynamic wetting of the structure is examined through high-speed imaging of a droplet interaction with the material structure. The high-speed camera (Phantom V711, vision research) is utilized in these experiments. Once a porous structure with positive imbibition parameter (i.e. hydrophilic surface) comes in contact with a fluid, the fluid impregnates quickly in the structure. The dynamics of the fluid flow to the structures is divided into two regimes: (i) inertia dominant region and (ii) viscous dominant region. This dynamics depends on radius of the channels in the structure, interfacial properties of the solid and liquid and the hydrodynamic properties of the fluid. We have used this dynamics to determine the average size of the interconnected veins in the structure. We placed a water droplet on the surface of the structure and examined its dynamic as shown in **Fig. 2b**. A movie of the droplet interaction with the material structure at 30 frame/s is included. We consider that the fluid flow in the structure is mostly viscous dominant and use the Washburn's law to determine the average size of the veins in the structure written as

$$\boldsymbol{z^2(t) = \frac{1}{2}\frac{\gamma R \cos\theta}{\mu} t,} \tag{A3}$$

where $\boldsymbol{z}$ denotes the length-scale of impregnation, $\boldsymbol{\gamma}$ liquid-vapor surface tension, $\boldsymbol{R}$ the average dimension of the channels, $\boldsymbol{\theta}$ contact angle, and $\boldsymbol{\mu}$ the viscosity of the fluid. We determined the impregnation length through the volume of the droplet divided by the wetted area. Also, the contact angle of the water on the exfoliated graphite surface measured in Ghasemi et al.[27] is 40^o. The average size of the channels is 30 ± 10 μm. Also, we can take the derivative of the Washburn's law to calculate the velocity of the fluid

once it reaches the surface of the structure. This velocity is ~ 10 cm/s. If we consider no change in the interfacial properties at high solar illumination, the maximum electromagnetic illumination on the surface without drying is written as

$$\dot{\boldsymbol{q}} = \boldsymbol{h_{fg}}\, \boldsymbol{\rho}\, \boldsymbol{V}, \tag{A4}$$

where $\dot{\boldsymbol{q}}$ denotes the electromagnetic flux, $\boldsymbol{h_{fg}}$ enthalpy of phase change, $\boldsymbol{\rho}$ density of fluid, and $\boldsymbol{V}$ velocity of fluid in the veins at the surface of the structure. Thus, the structure can sustain the fluid flow to the surface even up to high intensity of electromagnetic illumination in order of 10^5 kWm^{-2} without drying.

APPENDIX V: Thermal Conductivity Measurements

Thermal conductivity of the structure is measured through IR method. In this approach, the structure is sandwiched between two reference glass slabs with known thermal conductivity. A resistance heater is attached to the top glass slab and the current through the heater is tuned to introduce a range of temperature gradient across the sample. The setup is placed in front of an IR camera with resolution of 25 μm to measure the temperature gradient in the glass slabs and the sample. The IR camera is calibrated by measurement of the emissivity map in an isothermal condition. As the thermal conductivity of the reference material is known, the measured temperature gradient in the glass slab is used to determine the heat flux to the sample. Given the heat flux and the temperature gradient in the material, thermal conductivity of the material is determined through Fourier equation. The linear correlation of heat flux and temperature gradient suggests a negligible contribution of convection losses by the sides in the measurements.

APPENDIX VI: Chemical Stability of the Material Structure

To examine the chemical stability of structure, we prepared a range of solutions in PH range of 1-11. The acidic solutions are prepared through various HCL and water concentrations. The basic solutions are Tris 0.15 mM NaCL (PH=8) and Sodium Phosphate (PH=11) solutions. We soaked the structure in these solutions for 18 hrs. **Figure 6** shows the structure before and after each experiment. No change in the integrity of the structure is observed.

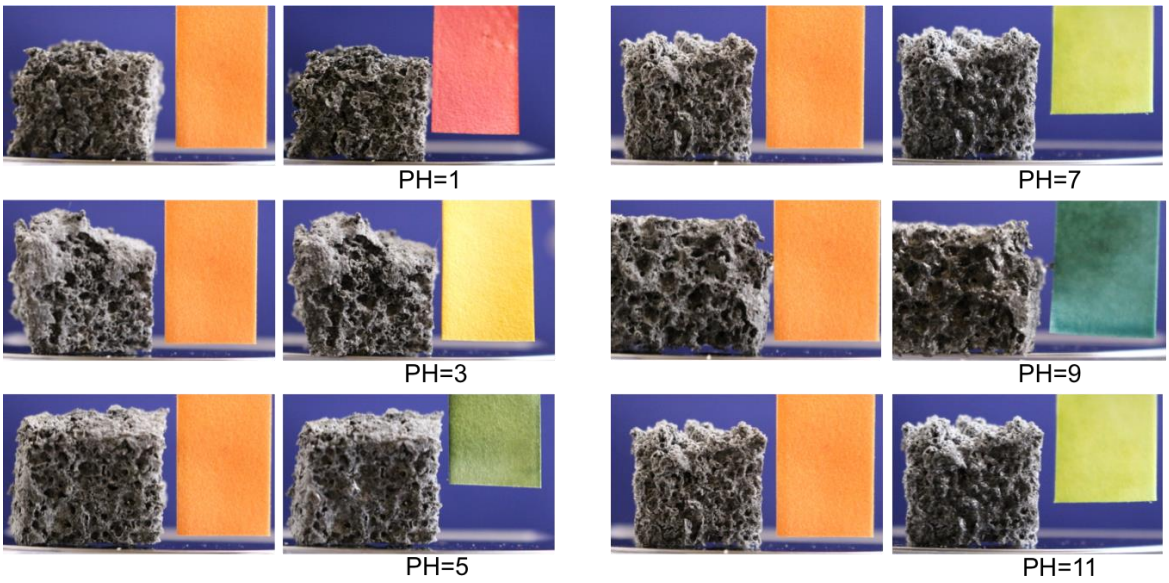

Figure 6. The developed material structure was examined in a range of chemical solutions with the PH range of 1-11. The structure before and after each experiment is shown. No change in the integrity of the structure was observed.

APPENDIX VII: Experimental Setup

The experimental setup in this work is specifically designed to assess performance of the structure at low and high steam pressures. As shown in **Fig. 7**, the experimental setup includes (1) a cylindrical chamber with diameter of 25.4 mm with an attached flange on top; (2) the glass flange (Archon Industries, tempered borosilicate glass) that can withstand up to high pressure of 40 bar; (3) a solar simulator equipped with an optical head with maximum concentration of 50 kWm^{-2}, (OAI 0131-0293-01 with Aluminum mirror and 1.6 kW lamp); (4) a power measurement system consisting of a Newport thermopile detector (919P-500-65, 500W, 65 mm diameter) and Newport power meter (1918-R); (5) thermocouples type T for measurement of liquid and vapor temperatures, (6) A pressure gauge (Prosense, SPT25-20-0500A) to measure the pressure of the generated steam, (7) a syringe pump (Kd Scientific) to supply the liquid to the chamber; (8) and a data acquisition system (National Instruments, NI USB-6210).

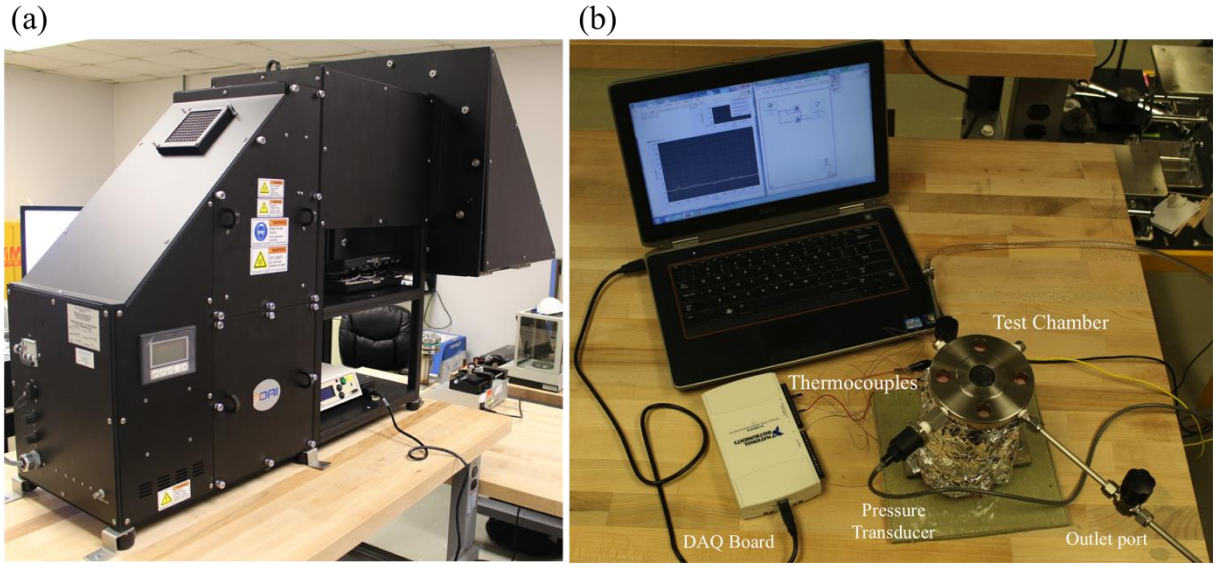

Figure 7. The experimental setup for ambient and high-pressure solar steam generation. (a) The solar simulator with the optical head enables us to conduct the experiments in the solar concentration range of 1-50 kWm^{-2}. (b) The measurement instrument and the test chamber are shown.

The cylindrical chamber is covered with fiberglass insulation to minimize the 2D side losses. The chamber has one inlet and one outlet. The inlet of the chamber is connected to the syringe pump through a piping system. The outlet of the chamber is left open for removal of generated steam. The syringe pump provides the ability to measure the evaporation rate of water accurately in a steady-state condition. The thermocouples and pressure gauge are calibrated before the experiments. The thermocouple in the vapor phase is placed at approximately 1 mm on top of the structure. This thermocouple is coated with a white coating to suppress the effect of direct illumination on the temperature measurements. The thermocouples in the liquid phase are placed underneath of the structure with intervals of 15 mm. All the thermocouples and the pressure gauge are connected to the Data Acquisition system and the generated data is collected by a LabView program. The solar intensity at the surface of the structure is measured with the Newport

thermopile. Each measurement of the solar intensity is repeated three times and the average measured value is reported. The standard deviation in the measurements of solar irradiation is less than 2%. We have used a highly reflective aperture with diameter of 25 mm on top of the test chamber to form a circular solar illumination spot with the same inside diameter of test chamber. All the experiments were conducted for long time to reach steady-state condition.

APPENDIX VIII: Parasitic Heat Losses by the Experimental Setup

The parasitic loss of the experimental setup is determined through simulation in COMSOL. The temperature of the generated steam at ambient pressure for pure graphite and DLS is shown in **Fig 8**. In all the structures, the generated steam reaches to 100 ^{o}C. The energy dissipated through surface convection, radiation, and heat losses to the experimental setup is only a function of structure temperature (i.e. close to steam temperature) and will be the same for all the structures. The difference between the performances of different structures is heat dissipated to the underlying liquid.

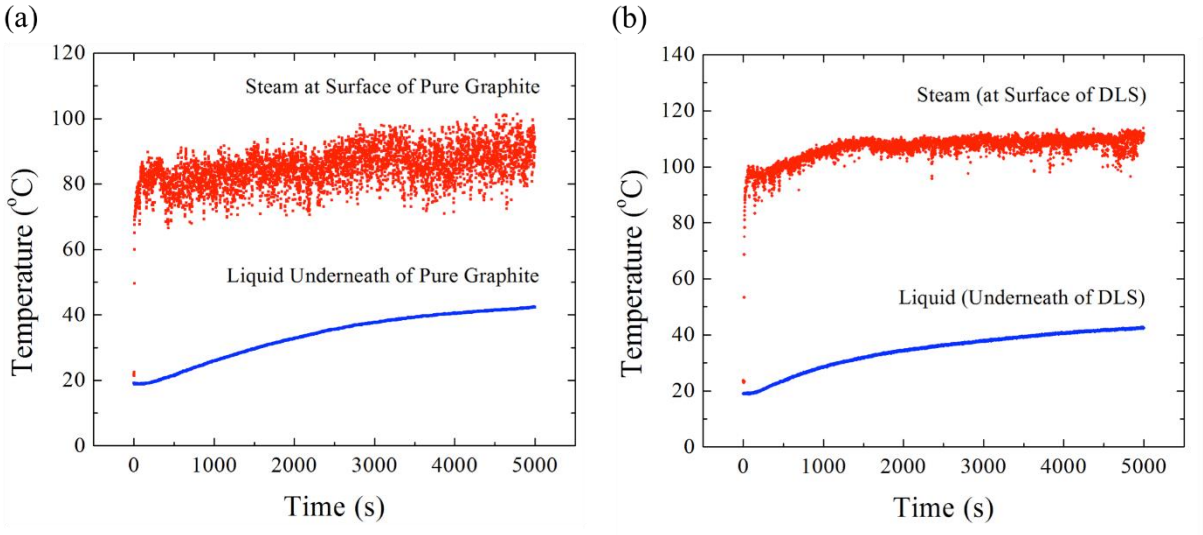

Figure 8. Temperature of the generated steam and underlying liquid for different structures are shown. For both pure graphite and DLS, the generated steam reaches to temperature of 100 ^{o}C. However, DLS has shorter transient time.

Assuming the temperature of top of the structure is close to the steam temperature, we have determined heat dissipated to the experimental setup through the simulations. The simulated temperature map of the experimental setup is shown in **Fig. 9**. The boundary

condition in these simulations is convective heat transfer with coefficient of 10 $Wm^{-1}K^{-1}$. These simulations suggest that the experimental setup imposes the parasitic losses in the range of 38-44% under the solar concentration range of 12-40 kWm^{-2}.

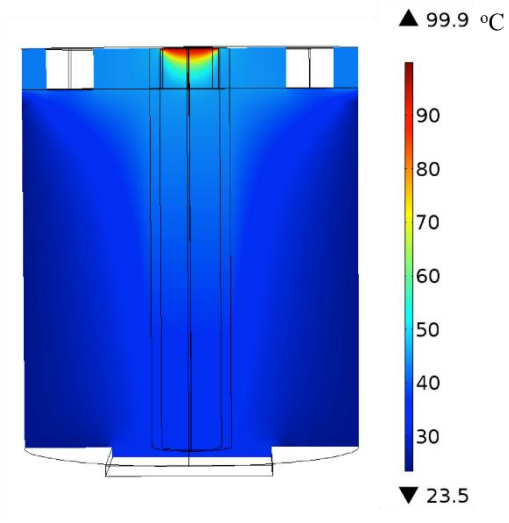

Figure 9. The temperature map of the cross-section of the experimental setup is shown. This experimental setup imposes up to 44% parasitic heat loss in the solar steam generation experiments.

APPENDIX IX: Energy Dissipation to the Bulk Liquid

As discussed above, the thermocouples in the bulk liquid were implemented to determine the energy dissipation to the underlying liquid. The transient temperature of liquid below the structure (< 2 mm gap between the thermocouple and the bottom of the structure) is compared between the developed structure herein and the other state-of-the-art structures. Lower temperature rise of the liquid is equivalent to better heat localization by the structure and consequently more efficient steam generation. These temperature trends are shown at various solar irradiations powers in **Fig. 10**.

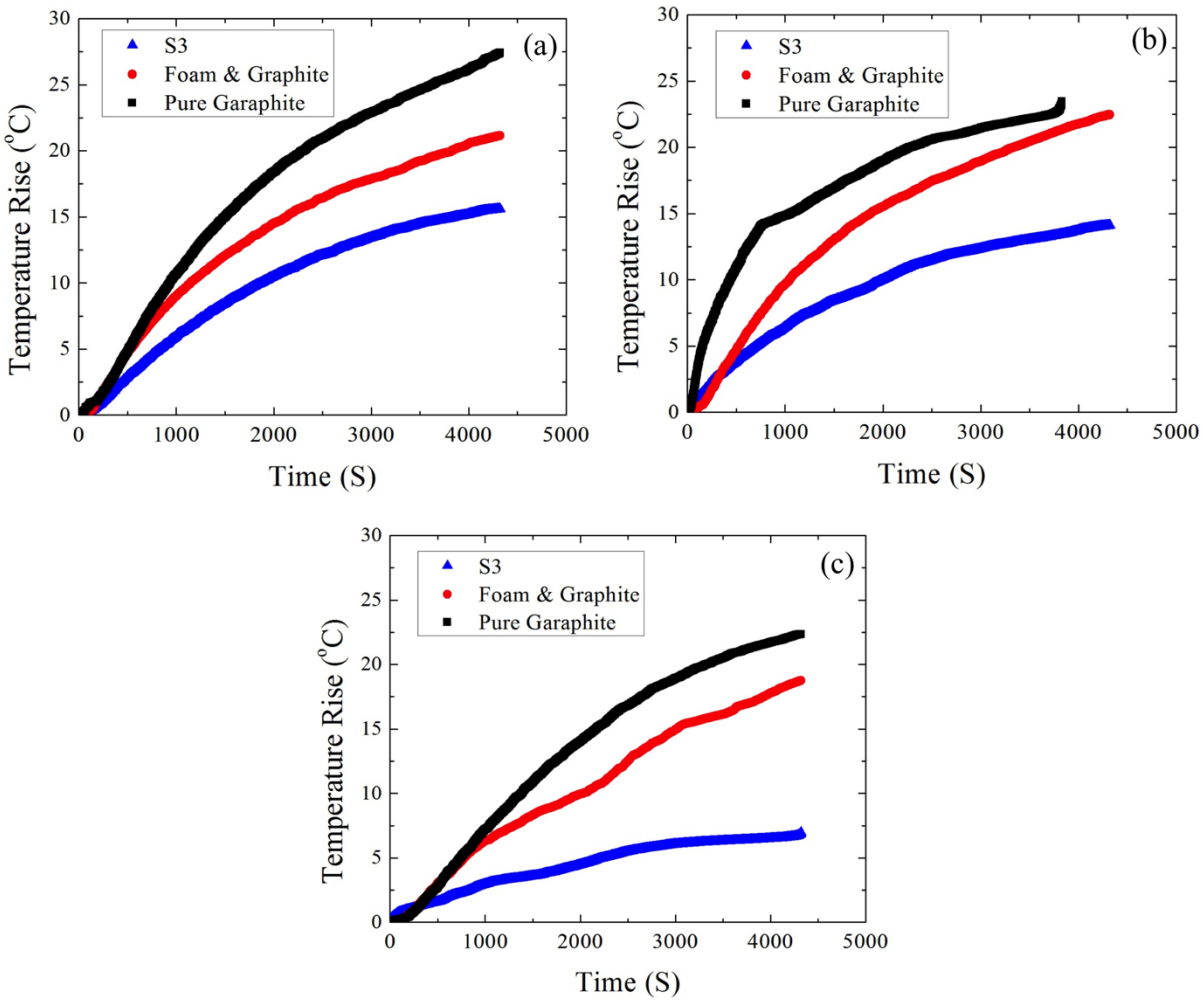

Figure 10. Temperature rise of the liquid below the structure is shown for different state-of-the-art structures at different solar irradiation power (a) 40 kWm^{-2}, (b) 30 kWm^{-2}, (c) 20 kWm^{-2}. Lower temperature rise indicates more heat localization by the structure and consequently higher efficiency of steam generation.

References

1 N. S. Lewis, *Science*, 2007, 315, 798–801.

2 S. Chu and A. Majumdar, *Nature*, 2012, 488, 294–303.

3 M. Romero and A. Steinfeld, *Energy Environ. Sci.*, 2012, 5, 9234.

4 T. Yamamoto, T. Furuhata, N. Arai and K. Mori, *Energy*, 2001, 26, 239–251.

5 World Health Organization, *The Burden of Health Care-Associated Infection Worldwide.*, 2010.

6 World Health Organization, *Solar Powered Autoclaves*, 2010.

7 J. P. Clark, *Food Technol.*, 2010, 91–93.

8 H. Tyagi, P. Phelan and R. Prasher, *J. Sol. Energy Eng.*, 2009, 131, 041004.

9 T. P. Otanicar, P. E. Phelan, R. S. Prasher, G. Rosengarten and R. a. Taylor, *J. Renew. Sustain. Energy*, 2010, 2, 033102.

10 G. Ni, N. Miljkovic, H. Ghasemi, X. Huang, S. V. Boriskina, C.-T. Lin, J. Wang, Y. Xu, M. M. Rahman, T. Zhang and G. Chen, *Nano Energy*, 2015, 17, 290–301.

11 R. a. Taylor, P. E. Phelan, T. P. Otanicar, C. a. Walker, M. Nguyen, S. Trimble and R. Prasher, *J. Renew. Sustain. Energy*, 2011, 3, 023104.

12 P. Phelan, R. Taylor, R. Adrian, R. Prasher and T. Otanicar, in *Nanoparticle Heat Transfer and Fluid Flow*, eds. W. J. Minkowycz, E. M. Sparrow and J. Abraham, CRC Press, 2012, pp. 123–142.

13 R. A. Taylor, P. E. Phelan, R. J. Adrian, A. Gunawan and T. P. Otanicar, *Int. J. Therm. Sci.*, 2012, 56, 1–11.

14 A. O. Govorov and H. H. Richardson, *Nano Today*, 2007, 2, 30–38.

15 E. Lukianova-Hleb, Y. Hu, L. Latterini, L. Tarpani, S. Lee, R. a Drezek, J. H. Hafner and D. O. Lapotko, *ACSNano*, 2010, 4, 2109–2123.

16 J. Lombard, T. Biben and S. Merabia, *Phys. Rev. Lett.*, 2014, 112, 105701.

17 G. Baffou, J. Polleux, H. Rigneault and S. Monneret, *J. Phys. Chem. C*, 2014, 118, 4890–4898.

18 G. Lajoinie, E. Gelderblom, C. Chlon, M. Böhmer, W. Steenbergen, N. de Jong, S. Manohar and M. Versluis, *Nat. Commun.*, 2014, 5, 3671.

19 N. J. Hogan, A. S. Urban, C. Ayala-Orozco, A. Pimpinelli, P. Nordlander and N. J. Halas, *Nano Lett.*, 2014, 14, 4640–4645.

20 D. T. Nguyen, R. Truong, R. Lee, S. A. Goetz and A. P. Esser-Kahn, *Energy Environ. Sci.*, 2014, 7, 2603.

21 S. V. Boriskina, H. Ghasemi and G. Chen, *Mater. Today*, 2013, 16, 375–386.

22 A. O. Govorov, W. Zhang, T. Skeini, H. Richardson, J. Lee and N. A. Kotov, *Nanoscale Res. Lett.*, 2006, 1, 84–90.

23 O. Neumann, A. S. Urban, J. Day, S. Lal, P. Nordlander and N. J. Halas, *ACS Nano*, 2013, 7, 42–9.

24 O. Neumann, C. Feronti, A. D. Neumann, A. Dong, K. Schell, B. Lu, E. Kim, M. Quinn, S. Thompson, N. Grady, P. Nordlander, M. Oden and N. J. Halas, *Proc. Natl. Acad. Sci. U. S. A.*, 2013, 110, 11677–81.

25 Z. Fang, Y.-R. Zhen, O. Neumann, A. Polman, F. J. García de Abajo, P. Nordlander and N. J. Halas, *Nano Lett.*, 2013, 13, 1736–42.

26 A. Polman, *ACSNano*, 2013, 7, 15–18.

27 H. Ghasemi, G. Ni, A. M. Marconnet, J. Loomis, S. Yerci, N. Miljkovic and G. Chen, *Nat. Commun.*, 2014, 5:4449.

28 Z. Wang, Y. Liu, P. Tao, Q. Shen, N. Yi, F. Zhang, Q. Liu, C. Song, D. Zhang, W. Shang and T. Deng, *Small*, 2014, 3234–3239.

29 S. Yu, Y. Zhang, H. Duan, Y. Liu, X. Quan and D. Tao, *Nat. Publ. Gr.*, 2015, 1–10.

30 Y. Liu, J. Chen, D. Guo, M. Cao and L. Jiang, *ACS Appl. Mater. Interfaces*, 2015, 7, 13645–13652.

31 Y. Ito, Y. Tanabe, J. Han, T. Fujita, K. Tanigaki and M. Chen, *Adv. Mater.*, 2015, 27, 4302–4307.

32 L. Zhang, B. Tang, J. Wu, R. Li and P. Wang, *Adv. Mater.*, 2015, 27, 4889–4894.

33 D. Zhao, H. Duan, S. Yu, Y. Zhang, J. He, X. Quan, P. Tao, W. Shang, J. Wu, C. Song and T. Deng, *Sci. Rep.*, 2015, 5, 17276.

34 K. Bae, G. Kang, S. K. Cho, W. Park, K. Kim and W. J. Padilla, *Nat. Commun.*, 2015, 6, 10103.

35 K. Zimny, A. Merlin, A. Ba, C. Aristégui, T. Brunet and O. Mondain-Monval, *Langmuir*, 2015, 31, 3215–3221.

36 N. R. Cameron, *Polymer (Guildf).*, 2005, 46, 1439–1449.

37 R. Zheng, J. Gao, J. Wang and G. Chen, *Nat. Commun.*, 2011, 2, 289.

38 L. M.-R. and M. O.-A. J. Vivas-Castro, G. Rueda-Morales, G. Ortega-Cervantez, J. Ortiz-López, in *Carbon Nanotubes - Synthesis, Characterization, Applications*, ed. S. Yellampalli, InTech, 2011, pp. 47–60.

Chapter 2

Decoupled hierarchical structures for suppression of Leidenfrost phenomenon

Abstract

Thermal management of high temperature systems is limited by the existence of the Leidenfrost point (LFP), at which the formation of a continuous vapor film between a hot solid and a cooling medium diminishes the heat transfer rate. This limit results in a bottleneck for the advancement of the wide spectrum of systems including electronics/photonics, reactors, and spacecraft. Here, we report new multi-scale decoupled hierarchical structures to completely eliminate the Leidenfrost phenomenon. This structure allows to independently tune the involved forces and to suppress LFP. Once a cooling medium contacts these surfaces, by re-routing the path of vapor flow, cooling medium remains attached to the hot solid substrates even at high temperatures (up to 570 ^{o}C) for heat dissipation through liquid-vapor phase change with no existence of Leidenfrost phenomenon. These new surfaces offer unprecedented heat dissipation capacity at high temperatures (two orders of magnitude higher than the other state-of-the-art surfaces).

1. Introduction

Evaporation and boiling are fundamental and core phenomena in a broad range of disciplines including power generation and refrigeration systems [1-8], desalination [9,10], electronic/photonic cooling [11-24], chemical reactors, aviation systems [25], and even biosciences [26-28]. Boiling heat transfer is characterized by the large dissipated heat flux for a small given superheat as it relies on the latent heat of the cooling fluid [29-32]. At low surface superheats, direct contact of the liquid with the solid substrate allows for very high heat dissipation capacity. However, at high surface superheat, formation of an insulating vapor layer at the solid-liquid interface limits the heat dissipation and the droplet levitates on a layer of vapor [33-40]. The onset temperature of this phenomenon is denoted by the Leidenfrost point (LFP) [41-45]. Under such conditions, the heat transfer rate is minimal and the temperature of the substrate can reach dangerous levels, such as those experienced in the Fukushima disaster. The limit of LFP has stalled abilities for thermal management of high-temperature devices and has impacted a broad spectrum of systems. The ability to raise LFP or to completely eliminate LFP opens a new path for breakthroughs in these systems.

1.1. Literature

A range of surface engineering approaches has been created to tune LFP. The earlier approaches included exploring different surface materials [46-48], tuning the roughness of surfaces [49-51], and using porous surfaces [52,53]. Recently, the dynamic field of nanotechnology has promised new avenues for surface engineering to tune LFP further. The later approaches included nanorough surfaces [54], nanofiber mats [55], micro/nano structured surfaces [56-63] and hierarchical surfaces [56-64]. In addition to surface engineering, other parameters such as tuning ambient pressure [65-67], chemical modification of the cooling medium [51,68-73], actuating inertia of the droplets[74-78] and active approaches (e.g. electrical fields [79-81]) are exploited to boost LFP. However, surface engineering is more appealing as other solutions are often constrained. We have summarized the reported LFP and their suggested physics for a water droplet with radius of 1.1-1.9 mm in Supplementary Information. The maximum reported LFPs of a water droplet is for hierarchical structures in value of 453 ^{o}C [64] and 400 ^{o}C [56]. In both of these structures, micro-pillars of Si were coated with nanoparticles (NPs) to provide a multi-scale structure to boost LFP. Kim et al. [64] suggested a mechanism for superior performance of hierarchical structures. Once a droplet approaches a hierarchical surface, if the thickness of the features on the surface is less than the thickness of the insulating vapor film, the features will only increase the shear resistance for vapor flow and consequently thicken the vapor film. In this case, the surface features do not play any role in the increase of LFP. However, as the droplet evaporates, the thickness of Leidenfrost film decreases with the rate of $R^{4/3}$ [45] and the droplet ultimately forms contact with the surface. Note

that R denotes the radius of the droplet. Upon contact, the heterogeneous nucleation of bubbles can occur if cavities are available for nucleation. To introduce these cavities on the surface, Kim et al.[64] used nano-particles on the micro-posts of hierarchical structures to show the role of these nano-features on the transition from film boiling to nucleate boiling. Thus, both length scales on the surface contribute to boost LFP. Despite a long time effort, a rational approach for complete suppression of LFP is missing. This suppression will be a breakthrough in thermal management of high-temperature systems.

2. Decoupled Hierarchal Structure

In the Leidenfrost phenomenon, the de-wetting upward force by vapor, which is caused by pressure gradient of the vapor flow underneath of the droplet, keeps the cooling droplet suspended and impedes contact of the droplet with the hot solid substrate. Here, we have developed a new paradigm and corresponding material structure for suppression of Leidenfrost phenomenon. Through decoupled hierarchical structures, we re-route the vapor flow and keep the cooling droplet in contact with the hot solid at extremely high temperatures. These new structures are composed of two sub-structures, a nano-membrane and a deep microstructure, **Fig. 1a**. Once a cooling droplet sits on the nano membrane, the generated vapor enters the deep microstructure and flows radially, while the nano membrane keeps the cooling droplet in contact with the hot solid through the capillary force. The de-wetting upward force by the vapor is only a function of dimensions of the microstructure, but downward capillary force, which keeps the droplet in contact with the hot solid, is only a function of pore dimensions in the nano membrane. Thus, as these forces are decoupled and independent, by tuning of these forces, the droplet can be kept in contact with the hot solid substrate even at high temperatures.

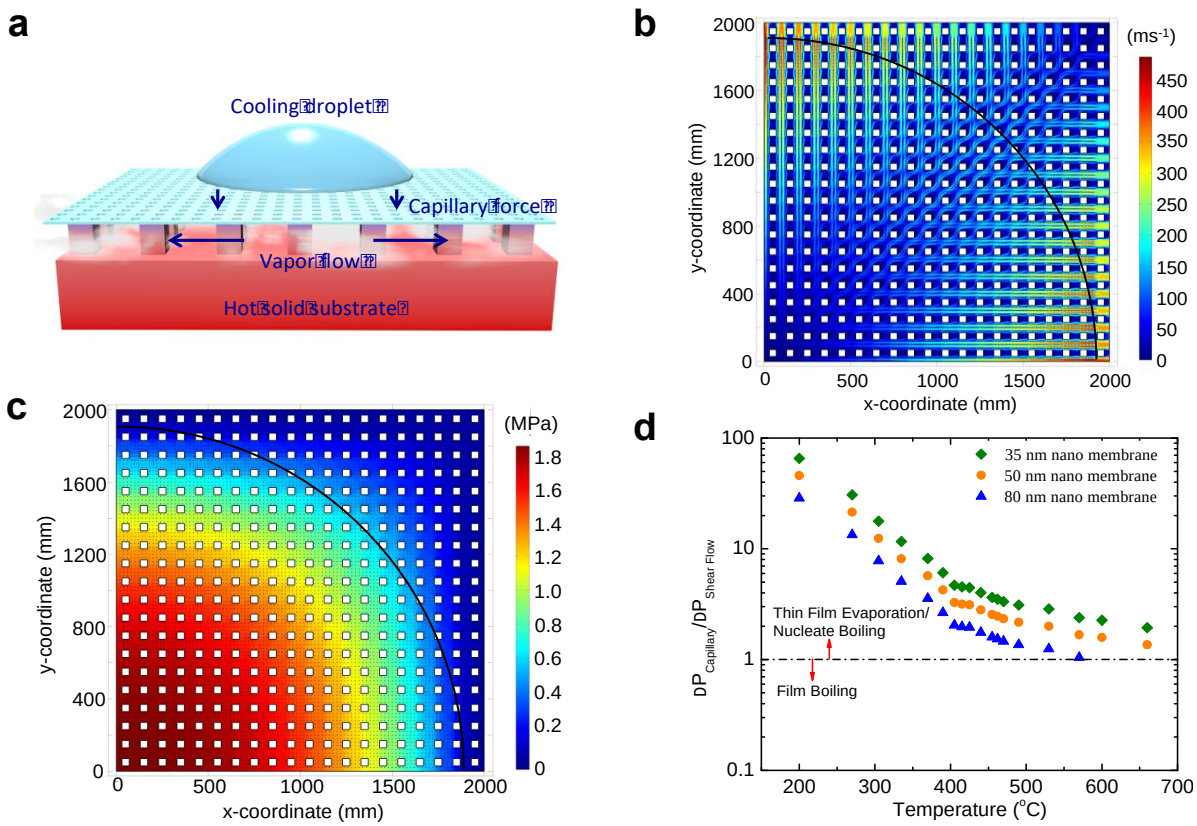

Figure 1. a) A schematic of decoupled hierarchical structure for suppression of Leidenfrost phenomenon is shown. b) The velocity field in the microstructure. c) The de-wetting pressure field by the vapor flow d) The ratio of de-wetting pressure to the capillary pressure as a function of temperature

In the Leidenfrost phenomenon, the insulating vapor layer impedes the direct contact of a cooling droplet and a hot substrate and significantly drops the dissipated heat flux. The thickness of static Leidenfrost film for small droplets is determined through the balance of interfacial mass flux and shear flow of vapor in the vapor film and is written as [45]

$$e = \left(\frac{k^v \, \Delta T \, \mu^v \, \rho_l \, g}{h_{fg} \, \rho_v \, \gamma^2}\right)^{1/3} R^{4/3}, \tag{1}$$

where k^v denotes the thermal conductivity of the vapor, ΔT the temperature difference between the solid substrate and the saturation temperature of liquid at the given pressure,

μ^v the viscosity of the vapor, ρ_l the density of liquid, g the gravitational acceleration, h_{fg} the enthalpy of the liquid-vapor phase change, ρ_v the density of vapor phase, and γ the surface tension of the liquid-vapor interface. For droplets with a radius larger than the capillary length, the thickness of Leidenfrost film is proportional to $R^{1/2}$.

The new advanced hierarchical structure herein changes the position of insulating vapor film and keeps the cooling droplet in contact with the hot solid substrate. As shown in **Fig. 1a**, the decoupled hierarchical structure includes a superhydrophilic nano membrane, which is joined on top of a deep Si micro-pillar structure. The height of pillars in the deep microstructure should be high enough to reduce the developed pressure by shear flow of the vapor in the microstructure. Through simulation of vapor flow, we found that the pillars with a height of > 95 μm is required to suppress LFP up to 570 ^{o}C (APPENDIX I Information, **Fig. 6**). Once a droplet contacts the nano membrane, the capillary force per unit area by the nano-pores, which is $\Delta P_{capillary} = 2\gamma \cos\theta / r_p$, keeps the droplet in contact with the nano membrane. Note that θ and r_p denote the contact angle of liquid meniscuses formed in the nano-pores and radius of the nano-pores, respectively. Consequently, liquid forms spherical meniscuses in the nano-pores as the dimension of nano-pores is much smaller than the capillary length of the liquid. At the liquid-vapor interface, evaporation occurs to dissipate heat flux by the hot solid substrate. The generated vapor flows in the microstructure radially and leaves the structure from the sides. Note that the shear loss for vapor upward flow through nano-pores is proportional to the thickness of the membrane divided by the dimension of the pores. This shear loss is 1-2 orders of magnitude higher than the shear loss through the microstructure. Thus, the generated vapor

flows predominantly radially in the microstructure. If the de-wetting force by vapor flow overcomes the capillary force, the droplet will detach from the substrate and adopt a Leidenfrost state. We should emphasize that these forces are decoupled and independent. The capillary force is a function of the characteristics of the nano membrane, while the de-wetting force by the vapor is a function of characteristics of microstructure. Thus, these forces can be modified independently to tune the LFP. We simulated the vapor flow in the microstructure to obtain an insight on pressure field of vapor. The details of simulation are given in the Supplementary Information. Also, we provide an approximate analytical solution of maximum pressure generated by the vapor flow in the Supplementary Information. In **Fig. 1b**, the velocity field of the vapor in the microstructure is shown. Although the vapor velocity reaches high values, the assumption of laminar flow field is still valid. Furthermore, we simulated the generated pressure field in the microstructure during the vapor flow as shown in **Fig. 1c**. If the maximum generated pressure in the microstructure is less than the induced capillary pressure by the nano membrane, the droplet will remain attached to the nano membrane and the Leidenfrost state is suppressed. Through these simulations, we can compare the ratio of pressures by the shear flow and the capillary phenomenon at different temperatures. This ratio is shown in **Fig. 1d** for several dimensions of nano membranes. Note that for a membrane with pore diameter of 80 nm, no Leidenfrost state will occur until a temperature of 570 ^{o}C.

As the microstructure is a deep microstructure (height of 95 ± 2 μm), we developed a custom-designed micro-fabrication approach for these structures. The details of this approach are provided in the Experimental Methods. The picture of the developed

microstructure is shown in **Fig. 2a**. We used Anodic Aluminum Oxide (AAO) as the nano membrane. These membranes with varied pore diameters were obtained from Synkera Technologies Inc. These membranes have a diameter of 25.4 mm, a thickness of 50 μm, and a pore density of 10%. We needed the contact angle of water in the nano-pores to determine capillary pressure in these pores. Once a water droplet is deposited on the nano membrane, the contact line rests on the flat area of the membrane and in some parts will be pinned by the nano-pores. As the covered area by the pores is only 10%, we consider that macro contact angle is not affected by the presence of the pores. As shown in **Fig. 2b**, we measured the contact angle of a water droplet on a pre-cleaned nano membrane and used this contact angle to determine the capillary pressure in the pores. The nano-membrane was cleaned with plasma cleaner (Harrick Plasma PDC-001-HP) before these measurements. The measured contact angle of a water droplet on these nano membranes is 3 ± 1^{o}. Thus, the membrane provides a superhydrophilic surface for the water droplet and once the liquid impregnates the nano pores, it adopts a lower contact angle. After fabrication of the microstructure, we used a sintering approach to attach the nano membrane to the Si micro pillars. A schematic of this approach is shown in APPENDIX II **Fig. 7**. In this approach, we utilized Au as the interlayer between the nano membrane and the micro-pillar structure [82]. One side of the nano membrane was coated with Au in the e-beam evaporator with a thickness of 300 nm. Also, the top of the micro pillars was coated with a thin layer of Au having a thickness of 500 nm. To open the nano pores, the nano membrane was physically etched using RIE180. The coated samples were assembled on

top of each other and a pressure of 2 MPa was applied to the sample. The sample was sintered at a temperature of 600 ^{o}C. The final structure is shown in **Fig. 2c**.

Once the decoupled hierarchical structure was developed, we examined the heat dissipation by these new structures.

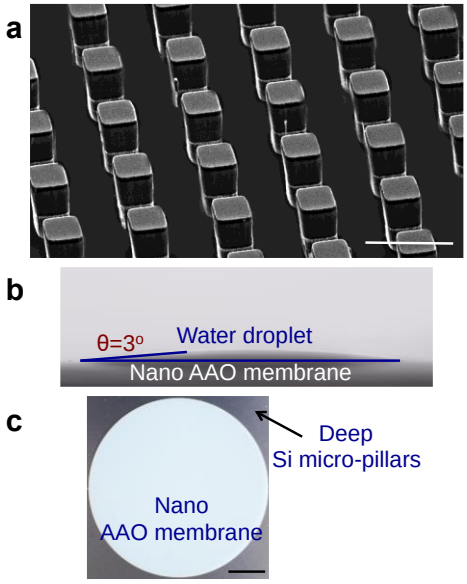

Figure 2. a) The structured of deep Si micro-pillar structures is shown. b) The contact angle of a water droplet on the AAO nano membrane is measured. c) The developed decoupled hierarchical structure is shown.

3. Result and Discussion

The experimental setup is developed as shown in the APPENDIX III **Fig. 8**. The decoupled hierarchical structure was thoroughly cleaned by plasma cleaning and was placed on the heating stage. Through fluid dispensing systems, droplets of DI water with a volume of 30 μL were introduced on the structure at a height of 4 mm (We~4.4). We minimized the distance between the droplet and the structure to suppress the role of droplet inertia on the droplet spreading. The temperature of the decoupled hierarchical structure was measured close to the droplet deposition coordinate with two independent thermocouples. These thermocouples are attached to the hierarchical structure with a thermal paste (OMEGA THERM 201). We measured the phase change characteristics of the water droplets as a function of temperature on these surfaces. These characteristics are captured using a high-speed camera (V711, Vision Research). As shown in **Fig. 3a**, at low value of superheat, the droplet is attached to the surface through the capillary force and thin film evaporation occurs underneath of the droplet. As the porosity of the studied membrane is only 10%, the evaporation rate of the droplet is small. As we increase the temperature, the phase-change characteristic enters a new regime in which nucleate boiling and thin-film evaporation occur simultaneously. Thus, the evaporation time of the droplet is reduced. We have shown the phase-change characteristics of a water droplet for four temperatures. Note that even up to a temperature of 540 ^{o}C, we did not observe the Leidenfrost phenomenon. We emphasize that the maximum measured Leidenfrost temperature on state-of-the-art surfaces is 453 ^{o}C [64]. The common approach to determine LFP and heat dissipation characteristics of a surface by a cooling sessile droplet is

measurement of the evaporation time as a function of temperature [83]. In **Fig. 3b**, we have plotted the water droplet evaporation time as a function of temperature on decoupled hierarchical structures. We developed these decoupled hierarchical structures with two nano membrane pore dimensions and examined their phase-change characteristics as shown in **Fig. 3b**. As the porosity of the nano membranes are the same, the difference in the evaporation rate cannot be related to the enhanced surface area for evaporation.

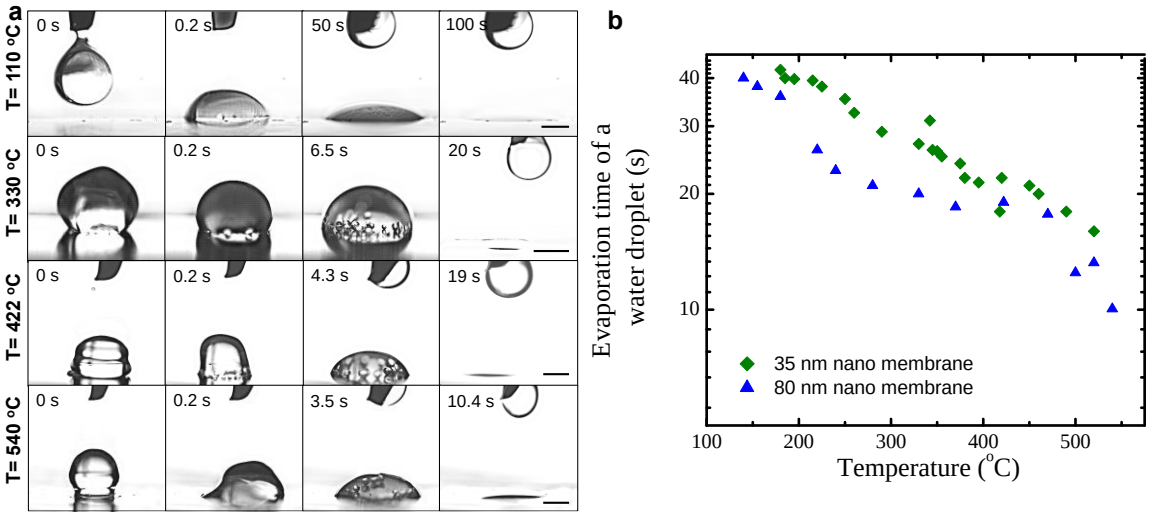

Figure 3. a) The phase-change characteristics of a water droplet on smooth decoupled hierarchical structure are shown. b) The droplet evaporation time by two types of decoupled hierarchical structure is measured. The evaporation time is a decreasing function of temperature.

We expect that the observed difference in the evaporation rate is caused by the non-uniform distribution of pores on the surface. As the characteristic curve shows, through decoupling of the de-wetting force of vapor flow and the capillary force, the Leidenfrost state is completely suppressed. However, the evaporation time of the droplets on these surfaces is higher than the state-of-the-art surfaces. This high evaporation time is caused by two parameters: low porosity of the nano membrane (10%) and consequently low surface area for phase-change and inadequate active site for heterogeneous nucleation of

vapor bubbles on the smooth nano membrane surface. To overcome this shortcoming of these smooth decoupled structures, we enhanced the nucleation sites of bubbles on the nano membranes through deposition of NPs. We deposited a layer of SiO_2 NPs on the decoupled hierarchical structure with nano pore dimension of 80 nm. The detail of the deposition approach is given in the Experimental Methods. Once the coated decoupled hierarchical structure is developed, we examined heat transfer characteristics of this structure on the heating stage. These characteristics are shown in **Fig. 4a**. Similar to the previous structures, we observed two regimes of phase-change. At low values of superheat, thin film evaporation at the mouth of the nano-pores occurs and the phase-change characteristics are similar to the decoupled hierarchical structures without coated NPs. However, as we increase temperature, the nucleation sites on the surface are activated and we observe the transition to the thin-film evaporation/boiling regime. The phase-change on these structures is more chaotic as enhanced boiling on the nano membrane surface occurs. We continued these experiments to a temperature of 570 ^{o}C. No LFP was observed on these decoupled hierarchical structures. The characteristics curve of evaporation time of a water droplet on these surfaces is shown in **Fig. 4b**. As shown, at high values of superheat the evaporation time on these surfaces is reduced by approximately two orders of magnitude. Nucleate boiling at the nano-membrane surface and evaporation at the mouth of nano-pores are responsible for this remarkable evaporation rate. We emphasize that the developed structures are sintered at 600 ^{o}C, and conducting experiments at higher temperatures (> 570 ^{o}C) would affect the integrity of the structure. However, once higher temperature joining approach is implemented, these structures can be operated at higher temperatures.

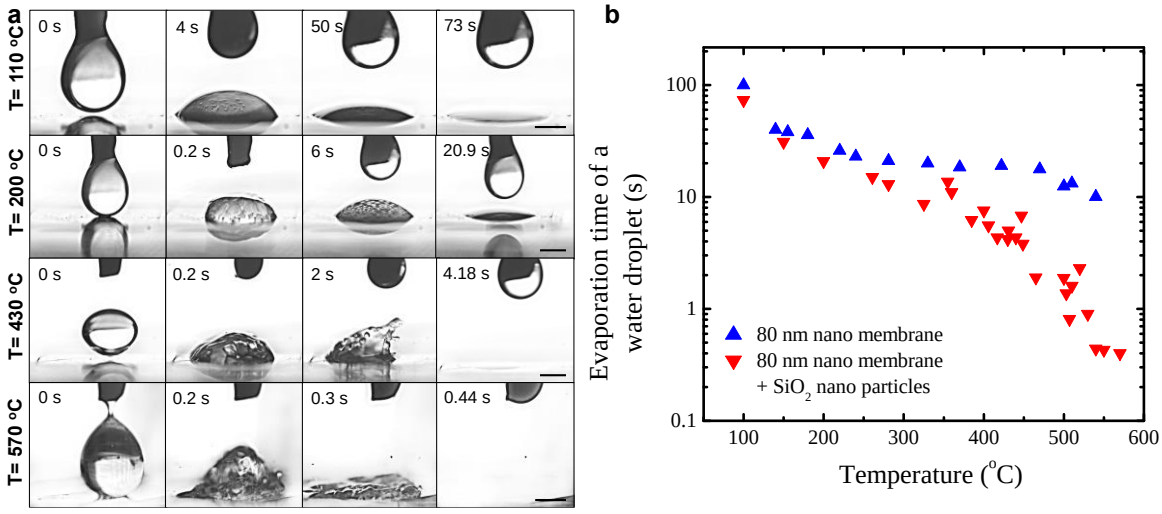

Figure 4. a) The phase-change characteristics of a water droplet on NP coated decoupled hierarchical structure at four temperatures are shown. b) The evaporation time of a water droplet on decoupled hierarchical structure and NP coated one are compared.

We compared heat transfer characteristics of the NPs coated decoupled hierarchical structure with other state-of-the-art surfaces as shown in **Fig. 5**. One of the structures is a hierarchical structure [64] in which Si micro-pillar structure is coated with SiO_2 NPs through layer-by-layer deposition. The procedure for this deposition was initially proposed by Iler [84] and further improved for aqueous solutions by Lee et al. [85] The onset of film boiling in this structure is at a temperature of 250 °C, and the LFP occurs at a temperature of 453 °C. The other state-of-the art structure is a zirconium nanotube structure [86], which is developed through anodic oxidation technique with hydrofluoric acid (0.5%). The onset of film boiling on this structure is close to 250 °C and LFP occurs at a temperature of 350 °C. We emphasize that LFP of around 400 °C is also reported by kwon et al. [56] in Si hierarchical structures, but the characteristic curve of evaporation time was not reported. As shown, the developed decoupled hierarchical structure in this work shows a distinct characteristic compared to the other structures. The Leidenfrost state in these structures is

suppressed up to temperature of 570 ^{o}C. The evaporation rate of a droplet and consequently the dissipated heat by these surfaces is two orders of magnitudes higher the other state-of-the-art surfaces.

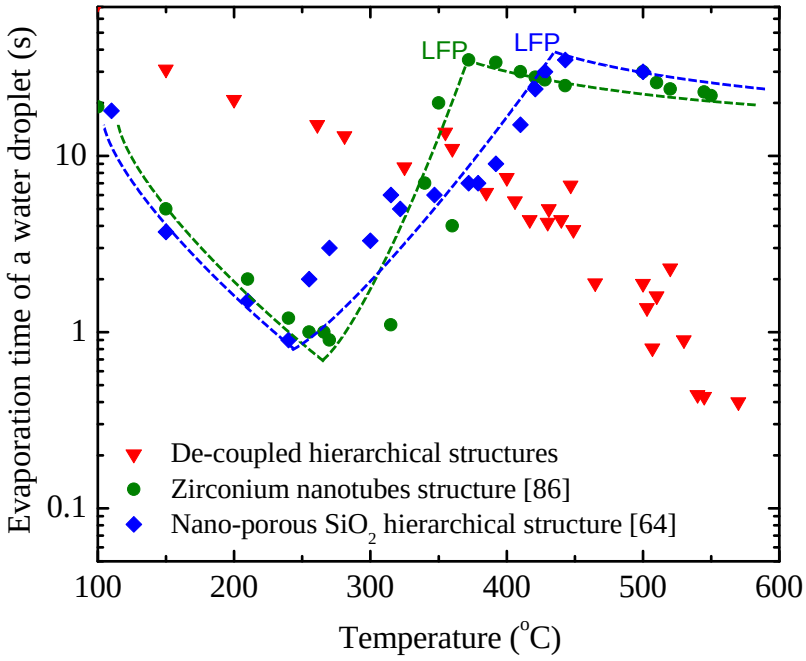

Figure 5. The phase-change characteristic on decoupled hierarchical structures is compared with state-of-the-art surfaces. On both other surfaces, LFP occurs which limits heat dissipation capacity by these surfaces.

4. Conclusions

In conclusion, we have presented a new paradigm for heat dissipation at high temperatures and demonstrated the corresponding surface structure for suppression of Leidenfrost phenomenon. In these decoupled hierarchical structures, the de-wetting force by the vapor is governed by the microstructure while the capillary force is governed by the nano membrane. Through independent tuning of these forces, we have suppressed the formation of continuous vapor film underneath of a cooling droplet (Leidenfrost phenomenon). These novel structures show two orders of magnitude higher heat dissipation capacity compared to other state-of-the-art surfaces. This is to our knowledge, the first reported surface with no Leidenfrost phenomena. These surfaces open a new path for thermal management of high power density systems and breakthroughs in power generation, chemical reactors, and aviation systems.

APPENDIX

APPENDIX I: Schematic of Microstructure

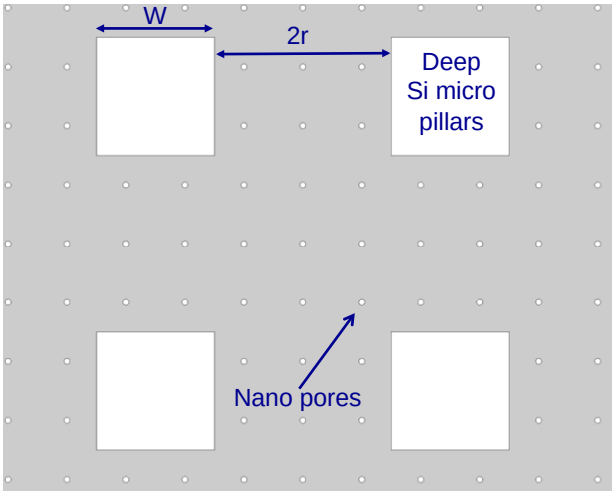

Figure 6. The top view of the developed model of vapor flow in the microstructure is shown. The model includes the nano-membrane, which is assembled on top of the micro-pillars. The generated vapor at the nano-pores flows in the microstructure radially and leaves the structure.

APPENDIX II: Schematic Figure of Decoupled Hierarchical Structure Fabrication

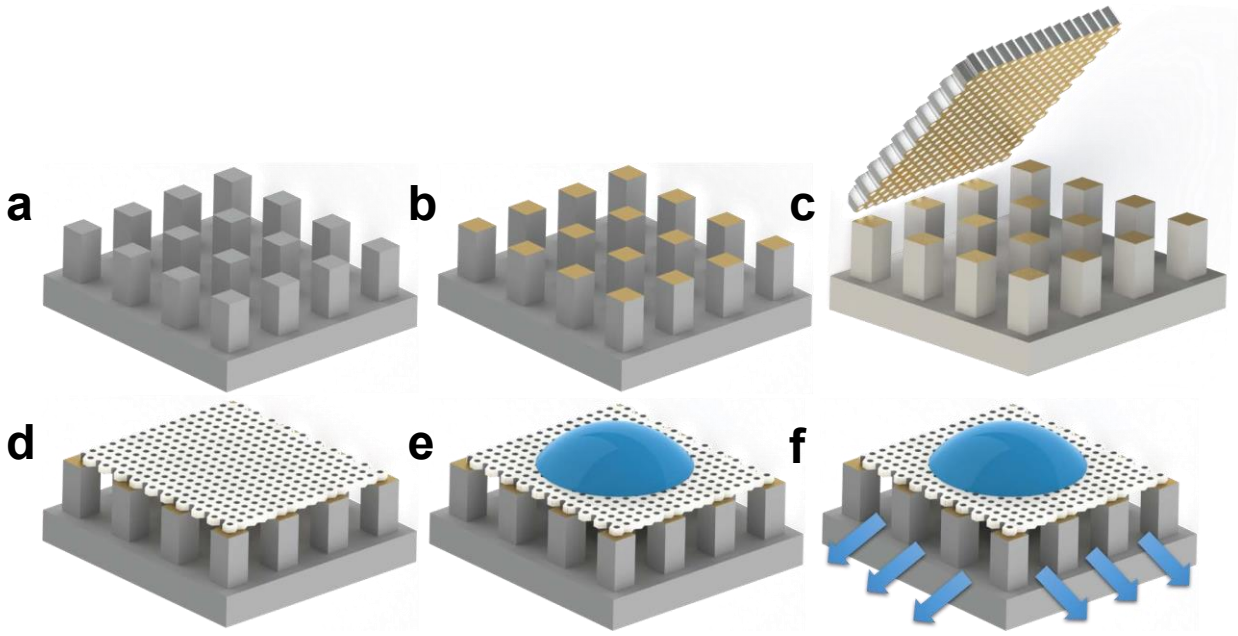

Figure 7. a) The deep Si microstructure was fabricated in the first step. b) A layer of Au film with thickness of 500 nm was coated on the pillars through e-beam evaporation c) The nano-membrane and the microstructure were assembled on top of each other. d) The structure was sintered

APPENDIX III: Experimental Setup

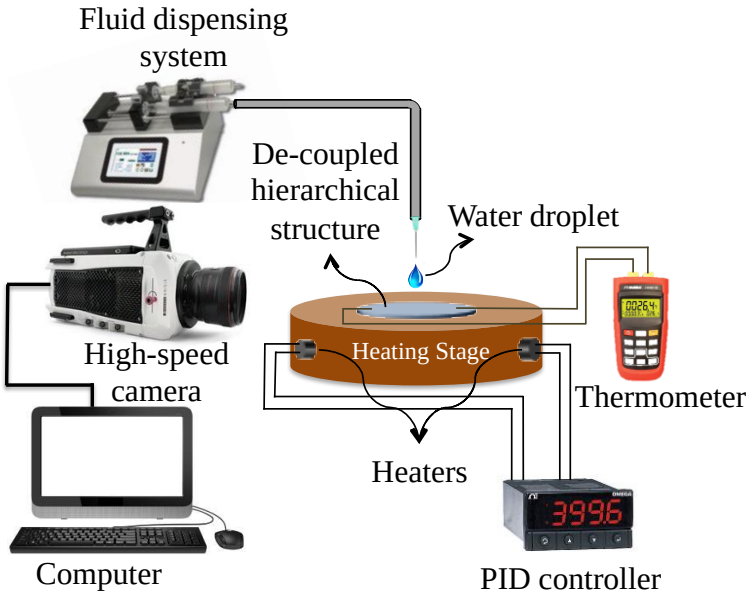

Figure 8. A water droplet with volume of 30 μl is deposited on the surface. The characteristics of the droplet are visualized with a high-speed camera. The temperature of the surface is measured with two independent thermocouples. The temperature of the heating stage is controlled with a PID controller.

APPENDIX IV: Heat Flux Comparison

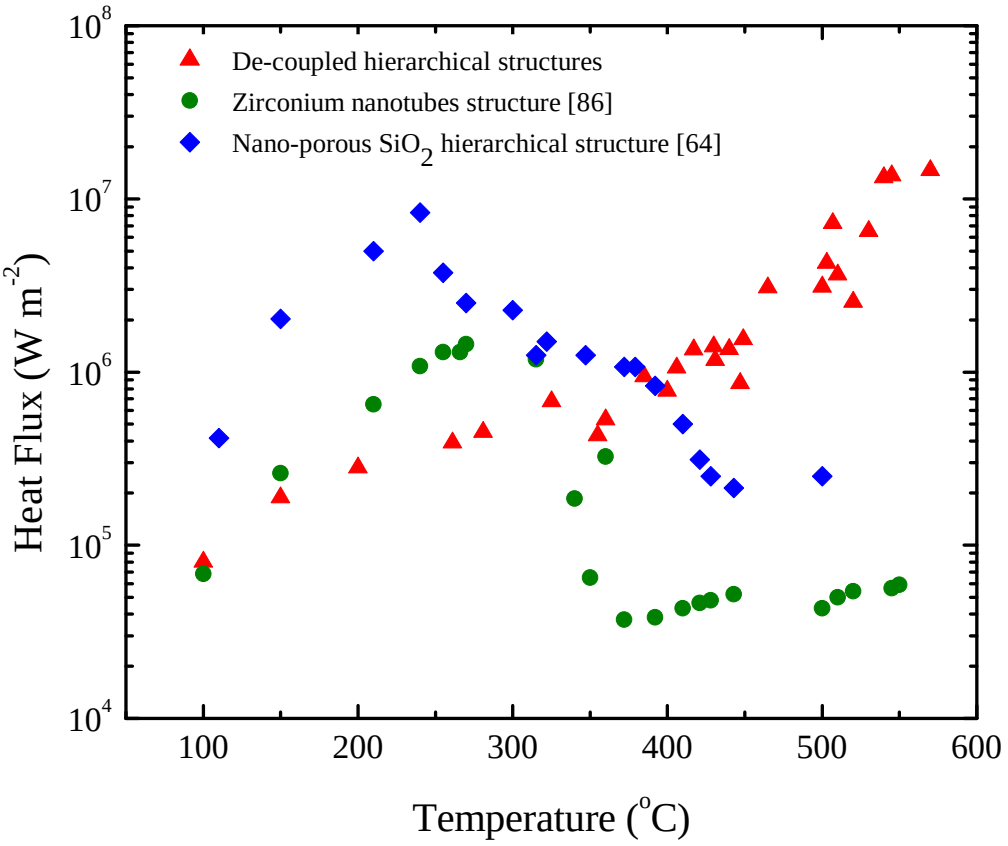

Figure 9. Heat flux by the decoupled hierarchical structure is compared with other state-of-the-art surfaces. The heat flux is determined through the evaporation time of the droplet and the contact area at different temperatures.

APPENDIX V: LEIDENFROST LIMIT

The reported LFP and their suggested physics for a water droplet with radius of 1.1-1.9 mm is summarized in Table 1.

Table 1. The reported surfaces to boost LFP

Approach	Fluid	Method	LFP limit (°C)
De-coupled hierarchical structures (This work)	DI Water	Passive	No limit was found.
Hierarchical structures, Nano SiO_2 on Si posts[1]	DI Water	Passive	453
Hierarchical Si structure[2]	DI Water	Passive	400
Zirconium nanotube[3]	DI Water	Passive	370
Polymer nanofiber mats[4]	DI Water	Passive	300
Salt deposition on surface[5]	DI Water + KCl	Passive	280
Salts increased surface roughness[6]	DI Water + $MgSO_4$	Passive	240

APPENDIX VI: SIMULATIONS

We developed a model of these decoupled hierarchical structures as shown in **Fig. 6**. The model includes the pillars with width of 40 μm, pitch of 60 μm between pillars, and height of 95 μm. The boundary conditions are the outlet pressure of the vapor (100 kPa) and symmetry boundary condition at the center of the droplet. As the droplet evaporates at the mouth of nano-pores, the generated vapor flows in the microstructure radially and leaves the structure from the sides. The velocity of the vapor at the nano-pores is the required input to the model. For this given velocity of vapor at the mouth of nano-pores, we can determine the velocity field in the microstructure and consequently the generated pressure field and maximum pressure of vapor underneath of the droplet. Comparison between this maximum pressure and capillary pressure defines the onset of LFP.

As discussed, we need to determine the velocity of generated vapor at the mouth of nano pores. The average vapor velocity from the energy balance at the liquid-vapor interface is written as

$$V_{nano-pore} \cong \frac{q\, w^2}{h_{fg}\, \rho_v\, (2r + w)^2\, \varrho}, \tag{1}$$

where q denotes the heat flux, w width of the micro pillars, h_{fg} the enthalpy of liquid-vapor phase change, ρ_v the density of vapor phase, $2r$ pitch between pillars, and ϱ the porosity of the nano membrane. The conductive heat flux to the liquid-vapor interface occurs through the micro-pillars. Thus, the heat flux can be approximated as $q = \Delta T / R_{th}$, where R_{th} is the thermal resistance of the decoupled hierarchical structure. This thermal resistance is written as

$$R_{th} = \frac{h}{k_{si}}, \tag{2}$$

where k_{si} denotes thermal conductivity of Si (149 $Wm^{-1}k^{-1}$). Note that we assume all the conducted heat through pillars is used in the evaporation process at the nano pores. For a given superheat of the substrate (ΔT), we determined the conducted heat flux to the liquid-vapor interface and consequently the average vapor velocity through Eq. (1). This average velocity was an input to the model to determine the onset of LFP for different nano-membrane dimensions, which is shown in **Fig. 1d**.

One can use an approximate analytical model to determine the maximum pressure drop generated by the vapor flow. The ratio of this shear pressure drop and capillary pressure determines the onset of LFP in the structure. The vapor flow in the microstructure can be modeled as a viscous dominated radial Poiseuille flow and the average velocity of vapor is written as

$$V_{microstructure} \cong \frac{q\ \lambda\ \varrho}{h_{fg}\ \rho_v\ h}, \tag{3}$$

where λ denotes length of the contact patch with the surface and h the height of pillars in the de-coupled hierarchical structure. The induced pressure gradient in the vapor phase is a result of two shear losses, one associated with the gradient of vapor velocity across the height of pillars, $\mu^v\ V/h^2$ and the other with velocity gradient across the pitch between pillars, $\mu^v\ V/w^2$. The viscosity of vapor is denoted by μ^v. The pressure gradient for the vapor flow is the superposition of these shear losses and is written as $\mu^v\ V(h^{-2} + w^{-2})$. Thus, one can write the de-wetting upward force per unit area by the vapor flow as

$$\Delta P_{shear} \approx \frac{\mu^{v}\, q\, \lambda\, l\, \varrho\, (h^{-2} + w^{-2})}{h_{fg}\, \rho^{V}\, h}, \tag{4}$$

where l denotes the length scale for radial flow of vapor, which is the width of the surface. We considered λ is equal to the pitch between pillars. The determined maximum pressure drop by the approximate analytical model is within 10% of the simulated model. Thus, one can use the analytical model to approximately determine the dimension of required nano-membrane for any given microstructure.

References

(1) Schmittinger, W.; Vahidi, A. A Review of the Main Parameters Influencing Long-Term Performance and Durability of PEM Fuel Cells. *J. Power Sources* 2008, *180*, 1–14.

(2) Ghasemi, H.; Ni, G.; Marconnet, A. M.; Loomis, J.; Yerci, S.; Miljkovic, N.; Chen, G. Solar Steam Generation by Heat Localization. *Nat. Commun.* 2014, *5:4449*.

(3) Neumann, O.; Urban, A. S.; Day, J.; Lal, S.; Nordlander, P.; Halas, N. J. Solar Vapor Generation Enabled by Nanoparticles. *ACS Nano* 2013, *7*, 42–49.

(4) Nam, J. H.; Kaviany, M. Effective Diffusivity and Water-Saturation Distribution in Single- and Two-Layer PEMFC Diffusion Medium. *Int. J. Heat Mass Transf.* 2003, *46*, 4595–4611.

(5) Zeng, Y.; Yao, J.; Horri, B. A.; Wang, K.; Wu, Y.; Li, D.; Wang, H. Solar Evaporation Enhancement Using Floating Light-Absorbing Magnetic Particles. *Energy Environ. Sci.* 2011, *4*, 4074.

(6) Chen, X.; Goodnight, D.; Gao, Z.; Cavusoglu, A. H.; Sabharwal, N.; DeLay, M.; Driks, A.; Sahin, O. Scaling up Nanoscale Water-Driven Energy Conversion into Evaporation-Driven Engines and Generators. *Nat. Commun.* 2015, *6*, 7346.

(7) Neumann, O.; Feronti, C.; Neumann, A. D.; Dong, A.; Schell, K.; Lu, B.; Kim, E.; Quinn, M.; Thompson, S.; Grady, N.; *et al.* Compact Solar Autoclave Based on Steam Generation Using Broadband Light-Harvesting Nanoparticles. *Proc. Natl. Acad. Sci. U. S. A.* 2013, *110*, 11677–11681.

(8) Sajadi, S. M.; Farokhnia, N.; Irajizad, P.; Hasnain, M.; Ghasemi, H. Flexible

Artificially Networked Structure for Ambient/high Pressure Solar Steam Generation. *J. Mater. Chem. A* 2016, *4*, 4700–4705.

(9) Elimelech, M.; Phillip, W. A. The Future of Seawater and the Environment: Energy, Technology, and the Environment. *Science* 2011, *333*, 712–718.

(10) Ng, K. C.; Thu, K.; Oh, S. J.; Ang, L.; Shahzad, M. W.; Ismail, A. Bin. Recent Developments in Thermally-Driven Seawater Desalination: Energy Efficiency Improvement by Hybridization of the MED and AD Cycles. *Desalination* 2015, *356*, 255–270.

(11) Wang, H.; Garimella, S. V.; Murthy, J. Y. An Analytical Solution for the Total Heat Transfer in the Thin-Film Region of an Evaporating Meniscus. *Int. J. Heat Mass Transf.* 2008, *51*, 6317–6322.

(12) Jiao, A. J.; Ma, H. B.; Critser, J. K. Evaporation Heat Transfer Characteristics of a Grooved Heat Pipe with Micro-Trapezoidal Grooves. *Int. J. Heat Mass Transf.* 2007, *50*, 2905–2911.

(13) Narayanan, S.; Fedorov, A. G.; Joshi, Y. K. On-Chip Thermal Management of Hotspots Using a Perspiration Nanopatch. *J. Micromech. Microeng.* 2010, *20*, 075010.

(14) Plawsky, J. L.; Fedorov, a G.; Garimella, S. V; Ma, H. B. Nano- and Microstructures for Thin-Film Evaporation — A Review. *Nanosc. Microsc. Thermophys. Eng.* 2014, *18*, 251–269.

(15) Yan, C.; Ma, H. B. Analytical Solutions of Heat Transfer and Film Thickness in Thin-Film Evaporation. *J. Heat Transf.* 2013, *135*, 031501.

(16) Su, F.; Ma, H.; Han, X.; Chen, H.-H.; Tian, B. Ultra-High Cooling Rate Utilizing Thin Film Evaporation. *Appl. Phys. Lett.* 2012, *101*, 113702.

(17) Ma, H. B.; Cheng, P.; Borgmeyer, B.; Wang, Y. X. Fluid Flow and Heat Transfer in the Evaporating Thin Film Region. *Microfluid. Nanofluid.* 2008, *4*, 237–243.

(18) Narayanan, S.; Fedorov, A. G.; Joshi, Y. K. Interfacial Transport of Evaporating Water Confined in Nanopores. *Langmuir* 2011, *27*, 10666–10676.

(19) Dhavaleswarapu, H. K.; Garimella, S. V.; Murthy, J. Y. Microscale Temperature Measurements Near the Triple Line of an Evaporating Thin Liquid Film. *J. Heat Transfer* 2009, *131*, 61501.

(20) Migliaccio, C. P.; Dhavaleswarapu, H. K.; Garimella, S. V. Temperature Measurements near the Contact Line of an Evaporating Meniscus V-Groove. *Int. J. Heat Mass Transf.* 2011, *54*, 1520–1526.

(21) Cho, J.; Goodson, K. E. Thermal Transport: Cool Electronics. *Nat. Mater.* 2015, *14*, 136–137.

(22) Pop, E. Energy Dissipation and Transport in Nanoscale Devices. *Nano Res.* 2010, *3*, 147–169.

(23) Kandlikar, S. G.; Bapat, A. V. Evaluation of Jet Impingement, Spray and Microchannel Chip Cooling Options for High Heat Flux Removal. *Heat Trans. Eng.* 2007, *28*, 911–923.

(24) Farokhnia, N.; Irajizad, P.; Sajadi, S. M.; Ghasemi, H. Rational Micro/Nanostructuring for Thin-Film Evaporation. *J. Phys. Chem. C* 2016, *120*, 8742–8750.

(25) Meseguer, J.; Perez-Grande, I.; Sanz-Andres, A. *Spacecraft Thermal Control*; Woodhead Publishing, 2012.

(26) Yakhno, T. A.; Sedova, O. A.; Sanin, A. G.; Pelyushenko, A. S. On the Existence of Regular Structures in Liquid Human Blood Serum (Plasma) and Phase Transitions in the Course of Its Drying. *Tech. Phys.* 2003, *48*, 399–403.

(27) Trantum, J. R.; Baglia, M. L.; Eagleton, Z. E.; Mernaugh, R. L.; Haselton, F. R. Biosensor Design Based on Marangoni Flow in an Evaporating Drop. *Lab chip* 2014, *14*, 315–324.

(28) Dugas, V.; Broutin, J.; Souteyrand, E. Droplet Evaporation Study Applied to DNA Chip Manufacturing. *Langmuir* 2005, *21*, 9130–9136.

(29) Van P. Carey. *Liquid-Vapor Phase Change Phenomenon*; Taylor & Francis Group, LLC, 2008.

(30) Dhir, V. K. Boiling Heat Transfer. *Annu. Rev. Fluid Mech.* 1998, *30*, 365–401.

(31) Kandlikar, S. G. *Handbook of Phase Change: Boiling and Condensation*; CRC Press, 1999.

(32) Witte, L. Film Boiling from a Sphere. *Ind. Eng. Chem. Fundam.* 1968, *8*, 517–518.

(33) Adda-Bedia, M.; Kumar, S.; Lechenault, F.; Moulinet, S.; Schillaci, M.; Vella, D. Inverse Leidenfrost Effect: Levitating Drops on Liquid Nitrogen. *Langmuir* 2016, *32*, 4179–4188.

(34) Dodd, L. E.; Geraldi, N. R.; Xu, B. Bin; Mchale, G.; George, G.; Stuart-cole, S.; Martin, J.; Newton, M. I.; Wood, D. Low Friction Droplet Transportation on a Substrate with a Selective Leidenfrost Effect. *ACS Appl. Mater. Interfaces* 2016, *8*,

22658–22663.

(35) Dupeux, G.; Le Merrer, M.; Clanet, C.; Quéré, D. Trapping Leidenfrost Drops with Crenelations. *Phys. Rev. Lett.* 2011, *107*, 1–4.

(36) Linke, H.; Alemán, B. J.; Melling, L. D.; Taormina, M. J.; Francis, M. J.; Dow-Hygelund, C. C.; Narayanan, V.; Taylor, R. P.; Stout, a. Self-Propelled Leidenfrost Droplets. *Phys. Rev. Lett.* 2006, *96*, 2–5.

(37) Vakarelski, I. U.; Marston, J. O.; Chan, D. Y. C.; Thoroddsen, S. T. Drag Reduction by Leidenfrost Vapor Layers. *Phys. Rev. Lett.* 2011, *106*, 3–6.

(38) Lagubeau, G.; Le Merrer, M.; Clanet, C.; Quéré, D. Leidenfrost on a Ratchet. *Nat. Phys.* 2011, *7*, 395–398.

(39) Hashmi, A.; Xu, Y.; Coder, B.; Osborne, P. a; Spafford, J.; Michael, G. E.; Yu, G.; Xu, J. Leidenfrost Levitation: Beyond Droplets. *Sci. Rep.* 2012, *2*, 797.

(40) Snoeijer, J. H.; Brunet, P.; Eggers, J. Maximum Size of Drops Levitated by an Air Cushion. *Phys. Rev. E - Stat. Nonlinear, Soft Matter Phys.* 2009, *79*, 1–13.

(41) Leidenfrost, J. G. *De Aquae Communis Nonnullis Qualitatibus Tractatus, Duisburg on Rhine*; 1765.

(42) Quéré, D. Leidenfrost Dynamics. *Annu. Rev. Fluid Mech.* 2013, *45*, 197–215.

(43) Nukiyama, S. The Maximum and Minimum Values of the Heat Q Transmitted from Metal to Boiling Water under Atmospheric Pressure. *Int. J. Heat Mass Transf.* 1966, *9*, 1419–1433.

(44) Burton, J. C.; Sharpe, A. L.; Van Der Veen, R. C. A.; Franco, A.; Nagel, S. R. Geometry of the Vapor Layer under a Leidenfrost Drop. *Phys. Rev. Lett.* 2012, *109*,

1–4.

(45) Biance, A.-L.; Clanet, C.; Quéré, D. Leidenfrost Drops. *Phys. Fluids* 2003, *15*, 1632.

(46) Blaszkowska-Zakrzewska, H. Rate of Evaporation of Liquids from a Heated Metallic Surface. *Bull. Int. l'Academie Pol.* 1930, *4a-5a*, 188–190.

(47) Patel, B. M. The Leidenfrost Phenomenon for Extended Liquid Masses, 1965.

(48) Xiong, T. Y.; Yuen, M. C. Evaporation of a Liquid Droplet on a Hot Plate. *Int. J. Heat Mass Transf.* 1991, *34*, 1881–1894.

(49) Baumeister, K. J.; Henry, R. E.; Simon, F. F. Role of the Surface in the Measurement of the Leidenfrost Temperature. In *Augmentation of Convective Heat and Mass Transfer*; ASME: New York, 1970; pp. 91–100.

(50) Bernardin, J. D.; Stebbins, C. J.; Mudawar, I. Effects of Surface Roughness on Water Droplet Impact History and Heat Transfer Regimes. *Int. J. Heat Mass Transf.* 1997, *40*, 73–78.

(51) Cui, Q.; Chandra, S.; McCahan, S. The Effect of Dissolving Salts in Water Sprays Used for Quenching a Hot Surface: Part 2—Spray Cooling. *J. Heat Transfer* 2003, *125*, 333–338.

(52) Avedisian, C. T.; Koplik, J. Leidenfrost Boiling of Methanol Droplets on Hot Porous/ceramic Surfaces. *Int. J. Heat Mass Transf.* 1987, *30*, 379–393.

(53) Chandra, S.; Avedisian, C. T. Observations of Droplet Impingement on a Ceramic Porous Surface. *Int. J. Heat Mass Transf.* 1992, *35*, 2377–2388.

(54) Kim, H.; Buongiorno, J.; Hu, L. W.; McKrell, T. Nanoparticle Deposition Effects on the Minimum Heat Flux Point and Quench Front Speed during Quenching in

Water-Based Alumina Nanofluids. *Int. J. Heat Mass Transf.* 2010, *53*, 1542–1553.

(55) Weickgenannt, C. M.; Zhang, Y.; Sinha-Ray, S.; Roisman, I. V.; Gambaryan-Roisman, T.; Tropea, C.; Yarin, A. L. Inverse-Leidenfrost Phenomenon on Nanofiber Mats on Hot Surfaces. *Phys. Rev. E - Stat. Nonlinear, Soft Matter Phys.* 2011, *84*, 1–9.

(56) Kwon, H. M.; Bird, J. C.; Varanasi, K. K. Increasing Leidenfrost Point Using Micro-Nano Hierarchical Surface Structures. *Appl. Phys. Lett.* 2013, *103*, 2011–2016.

(57) Vakarelski, I. U.; Patankar, N. a.; Marston, J. O.; Chan, D. Y. C.; Thoroddsen, S. T. Stabilization of Leidenfrost Vapour Layer by Textured Superhydrophobic Surfaces. *Nature* 2012, *489*, 274–277.

(58) Liu, G.; Craig, V. J. Macroscopically Flat and Smooth Superhydrophobic Surfaces: Heating Induced Wetting Transitions up to the Leidenfrost Temperature. *Faraday Discuss.* 2010, *146*, 141–151.

(59) Kruse, C.; Anderson, T.; Wilson, C.; Zuhlke, C.; Alexander, D.; Gogos, G.; Ndao, S. Extraordinary Shifts of the Leidenfrost Temperature from Multiscale Micro/nanostructured Surfaces. *Langmuir* 2013, *29*, 9798–9806.

(60) Vakarelski, I. U.; Chan, D. Y. C.; Marston, J. O.; Thoroddsen, S. T. Dynamic Air Layer on Textured Superhydrophobic Surfaces. *Langmuir* 2013, *29*, 11074–11081.

(61) Agapov, R. L.; Boreyko, J. B.; Briggs, D. P.; Srijanto, B. R.; Retterer, S. T.; Collier, C. P.; Lavrik, N. V. Asymmetric Wettability of Nanostructures Directs Leidenfrost Droplets. *ACS Nano* 2014, *8*, 860–867.

(62) Arnaldo Del Cerro, D.; Marin, A. G.; Romer, G. R. B. E.; Pathiraj, B.; Lohse, D.;

Huis In ’T Veld, A. J. Leidenfrost Point Reduction on Micropatterned Metallic Surfaces. *Langmuir* 2012, *28*, 15106–15110.

(63) Adera, S.; Raj, R.; Enright, R.; Wang, E. N. Non-Wetting Droplets on Hot Superhydrophilic Surfaces. *Nat. Commun.* 2013, *4*, 2518.

(64) Kim, H.; Truong, B.; Buongiorno, J.; Hu, L. W. On the Effect of Surface Roughness Height, Wettability, and Nanoporosity on Leidenfrost Phenomena. *Appl. Phys. Lett.* 2011, *98*, 1–4.

(65) Testa, P.; Nicotra, L. Influence of Pressure on the Leidenfrost Temperature and on Extracted Heat Fluxes in the Transient-Mode and Low-Pressure. *J. Heat Transf. Asme* 1986, *108*, 916–921.

(66) Emmerson, G. S. The Effect of Pressure and Surface Material on the Leidenfrost. *Int. J. Heat Mss Transf.* 1975, *18*, 381–386.

(67) Orejon, D.; Sefiane, K.; Takata, Y. Effect of Ambient Pressure on Leidenfrost Temperature. *Phys. Rev. E - Stat. Nonlinear, Soft Matter Phys.* 2014, *90*, 1–6.

(68) Avedisian, C. T.; Fatehi, M. An Experimental Study of the Leidenfrost Evaporation Characteristics of Emulsified Liquid Droplets. *Int. J. Heat Mass Transf.* 1988, *31*, 1587–1603.

(69) Bertola, V. Drop Impact on a Hot Surface: Effect of a Polymer Additive. *Exp. Fluids* 2004, *37*, 653–664.

(70) Bertola, V. An Experimental Study of Bouncing Leidenfrost Drops: Comparison between Newtonian and Viscoelastic Liquids. *Int. J. Heat Mass Transf.* 2009, *52*, 1786–1793.

(71) Duursma, G.; Sefiane, K.; Kennedy, A. Experimental Studies of Nanofluid Droplets in Spray Cooling. *Heat Transf. Eng.* 2009, *30*, 1108–1120.

(72) Qiao, Y. M.; Chandra, S. Experiments on Adding a Surfactant to Water Drops Boiling on a Hot Surface. *Proc. R. Soc. A Math. Phys. Eng. Sci.* 1997, *453*, 673–689.

(73) Huang, C. K.; Carey, V. P. The Effects of Dissolved Salt on the Leidenfrost Transition. *Int. J. Heat Mass Transf.* 2007, *50*, 269–282.

(74) Bernardin, J. D.; Stebbins, C. J.; Mudawar, I. Mapping of Impact and Heat Transfer Regimes of Water Drops Impinging on a Polished Surface. *Int. J. Heat Mass Transf.* 1997, *40*, 247–267.

(75) Mehdizadeh, N. Z.; Chandra, S. Boiling during High-Velocity Impact of Water Droplets on a Hot Stainless Steel Surface. *Proc. R. Soc. A Math. Phys. Eng. Sci.* 2006, *462*, 3115–3131.

(76) Tran, T.; Staat, H. J. J.; Prosperetti, A.; Sun, C.; Lohse, D. Drop Impact on Superheated Surfaces. *Phys. Rev. Lett.* 2012, *108*, 1–5.

(77) Tran, T.; Staat, H. J. J.; Susarrey-Arce, A.; Foertsch, T. C.; van Houselt, A.; Gardeniers, H. J. G. E.; Prosperetti, A.; Lohse, D.; Sun, C. Droplet Impact on Superheated Micro-Structured Surfaces. *Soft Matter* 2013, *9*, 3272–3282.

(78) Wang, A.-B.; Lin, C.-H.; Chen, C.-C. The Critical Temperature of Dry Impact for Tiny Droplet Impinging on a Heated Surface. *Phys. Fluids* 2000, *12*, 1622–1625.

(79) Celestini, F.; Kirstetter, G. Effect of an Electric Field on a Leidenfrost Droplet. *Soft Matter* 2012, *8*, 5992.

(80) Shahriari, A.; Wurz, J.; Bahadur, V. Heat Transfer Enhancement Accompanying Leidenfrost State Suppression at Ultrahigh Temperatures. *Langmuir* 2014, *30*, 12074–12081.

(81) Welch, S. W. J.; Biswas, G. Direct Simulation of Film Boiling Including Electrohydrodynamic Forces. *Phys. Fluids* 2007, *19*.

(82) Jang, B.; Chen, X.-Z.; Siegfried, R.; Montero Moreno, J. M.; Özkale, B.; Nielsch, K.; Nelson, B. J.; Pané, S. Silicon-Supported Aluminum Oxide Membranes with Ultrahigh Aspect Ratio Nanopores. *RSC Adv.* 2015, *5*, 94283–94289.

(83) Bernardin, J. D.; Mudawar, I. The Leidenfrost Point: Experimental Study and Assessment of Existing Models. *J. Heat Transfer* 1999, *121*, 894.

(84) Iler, R. K. Multilayers of Colloidal Particles. *J. Colloid Interface Sci.* 1966, *21*, 569–594.

(85) Lee, D.; Rubner, M. F.; Cohen, R. E. All-Nanoparticle Thin-Film Coatings. *Nano Lett.* 2006, *6*, 2305–2312.

(86) Kim, S. H.; Seon Ahn, H.; Kim, J.; Kaviany, M.; Hwan Kim, M. Dynamics of Water Droplet on a Heated Nanotubes Surface. *Appl. Phys. Lett.* 2013, *102*.